


# Nobeyama 45 m mapping observations toward the nearby molecular clouds Orion A, Aquila Rift, and M 17: Project overview

Fumitaka NAKAMURA ,<sup>1,2,3,\*</sup> Shun ISHII ,<sup>1,4</sup> Kazuhito DOBASHI ,<sup>5</sup>  
Tomomi SHIMOIKURA ,<sup>5,6</sup> Yoshito SHIMAJIRI,<sup>1,7,8</sup> Ryohei KAWABE,<sup>1,2,3</sup>  
Yoshihiro TANABE,<sup>9</sup> Asha HIROSE,<sup>5</sup> Shuri OYAMADA,<sup>1,10</sup> Yumiko URASAWA,<sup>11</sup>  
Hideaki TAKEMURA,<sup>1,2</sup> Takashi TSUKAGOSHI,<sup>1</sup> Munetake MOMOSE,<sup>9</sup>  
Koji SUGITANI ,<sup>12</sup> Ryoichi NISHI,<sup>11</sup> Sachiko OKUMURA,<sup>10</sup> Patricio SANHUEZA,<sup>1</sup>  
Quang NYGEN-LUONG,<sup>1,13</sup> and Takayoshi KUSUNE<sup>1</sup>

<sup>1</sup>National Astronomical Observatory of Japan, 2-21-1 Osawa, Mitaka, Tokyo 181-8588, Japan

<sup>2</sup>The Graduate University for Advanced Studies (SOKENDAI), 2-21-1 Osawa, Mitaka, Tokyo 181-0015, Japan

<sup>3</sup>Department of Astronomy, The University of Tokyo, 7-3-1 Hongo, Bunkyo-ku, Tokyo 113-0033, Japan

<sup>4</sup>Joint ALMA Observatory, Alonso de Coórdova 3107 Vitacura, Santiago, Chile

<sup>5</sup>Department of Astronomy and Earth Sciences, Tokyo Gakugei University, 4-1-1 Nukuikitamachi, Koganei, Tokyo 184-8501, Japan

<sup>6</sup>Faculty of Social Information Studies, Otsuma Women's University, 12 Sanban-cho, Chiyoda-ku, Tokyo 102-8357, Japan

<sup>7</sup>Laboratoire AIM, CEA/DSM-CNRS-Université Paris Diderot, IRFU/Service d'Astrophysique, CEA Saclay, F-91191 Gif-sur-Yvette, France

<sup>8</sup>Department of Physics and Astronomy, Graduate School of Science and Engineering, Kagoshima University, 1-21-35 Korimoto, Kagoshima, Kagoshima 890-0065, Japan

<sup>9</sup>College of Science, Ibaraki University, 2-1-1 Bunkyo, Mito, Ibaraki 310-8512, Japan

<sup>10</sup>Faculty of Science, Department of Mathematical and Physical Sciences, Japan Women's University, 2-8-1 Mejirodai, Bunkyo-ku, Tokyo 112-8681, Japan

<sup>11</sup>Department of Physics, Niigata University, 8050 Ikarashi-2, Niigata 950-2181, Japan

<sup>12</sup>Graduate School of Natural Sciences, Nagoya City University, Mizuho-ku, Nagoya, Aichi 467-8601, Japan

<sup>13</sup>IBM Canada, 120 Bloor Street East, Toronto, ON, M4Y 1B7, Canada

\*E-mail: [fumitaka.nakamura@nao.ac.jp](mailto:fumitaka.nakamura@nao.ac.jp)

Received 2018 December 24; Accepted 2019 April 24

## Abstract

We carried out mapping observations toward three nearby molecular clouds, Orion A, Aquila Rift, and M 17, using a new 100 GHz receiver, FOREST, on the Nobeyama 45 m telescope. We describe the details of the data obtained such as intensity calibration, data sensitivity, angular resolution, and velocity resolution. Each target contains at least one high-mass star-forming region. The target molecular lines were  $^{12}\text{CO}$  ( $J = 1-0$ ),  $^{13}\text{CO}$  ( $J = 1-0$ ),  $\text{C}^{18}\text{O}$  ( $J = 1-0$ ),  $\text{N}_2\text{H}^+$  ( $J = 1-0$ ), and  $\text{CCS}$  ( $J_N = 8_7-7_6$ ), with which we covered the density range of  $10^2 \text{ cm}^{-3}$  to  $10^6 \text{ cm}^{-3}$  with an angular resolution of  $\sim 20''$  and a velocity resolution of  $\sim 0.1 \text{ km s}^{-1}$ . Assuming the representative distances of 414 pc, 436 pc, and

2.1 kpc, the maps of Orion A, Aquila Rift, and M 17 cover most of the densest parts with areas of about  $7 \text{ pc} \times 15 \text{ pc}$ ,  $7 \text{ pc} \times 7 \text{ pc}$ , and  $36 \text{ pc} \times 18 \text{ pc}$ , respectively. On the basis of the  $^{13}\text{CO}$  column density distribution, the total molecular masses are derived to be  $3.86 \times 10^4 M_{\odot}$ ,  $2.67 \times 10^4 M_{\odot}$ , and  $8.1 \times 10^5 M_{\odot}$  for Orion A, Aquila Rift, and M 17, respectively. For all the clouds, the  $\text{H}_2$  column density exceeds the theoretical threshold for high-mass star formation of  $\gtrsim 1 \text{ g cm}^{-2}$  only toward the regions which contain current high-mass star-forming sites. For other areas, further mass accretion or dynamical compression would be necessary for future high-mass star formation. This is consistent with the current star formation activity. Using the  $^{12}\text{CO}$  data, we demonstrate that our data have enough capability to identify molecular outflows, and for the Aquila Rift we identify four new outflow candidates. The scientific results will be discussed in detail in separate papers.

**Key words:** ISM: clouds — ISM: kinematics and dynamics — ISM: molecules — ISM: structure — stars: formation

## 1 Introduction

Star formation not only determines the observed properties of galaxies, but also significantly influences galaxy evolution (Mac Low & Klessen 2004; McKee & Ostriker 2007). What drives and regulates star formation in galaxies? There is little consensus to this apparently simple and fundamental question. Theoretical studies have demonstrated that once self-gravitating objects (cloud cores) form, their gravitational collapse leads to star formation at high rates (Klessen et al. 1998). However, star formation is known to occur at a very low rate in galaxies (Zuckerman & Evans 1974). For example, the total molecular gas mass in our Galaxy is estimated to be  $10^9 M_{\odot}$  from CO observations. If all the molecular clouds are converted to stars within a cloud free-fall time which is a few Myr at the typical cloud density of a few thousand  $\text{cm}^{-3}$ , the *free fall* rate of star formation is calculated to be about  $10^3 M_{\odot} \text{ yr}^{-1}$ , which is about  $10^3$  times larger than the observed star formation rate (McKee & Williams 1997; Murray & Rahman 2010; Robitaille & Witney 2010). More accurate estimations of star formation rates toward individual molecular clouds are basically consistent with the above rough calculation (Krumholz & Tan 2007). The small Galactic star formation rate thus implies that some physical processes make star formation slow and inefficient.

However, it remains uncertain exactly what processes make star formation slow and inefficient. Several have been discussed as slowing down and regulating star formation, e.g., stellar feedback, magnetic field, and cloud turbulence (Shu et al. 1987; McKee & Ostriker 2007; Krumholz et al. 2014). It is thus crucial to characterize the internal cloud structure and physical properties of nearby molecular clouds to understand the roles of these processes in star formation. In our project, we carried out mapping observations toward three nearby molecular clouds using

the Nobeyama 45 m telescope, and attempt to address the issues of inefficient star formation.

Star formation processes are often influenced by large-scale events. Protostellar jets and outflows are often extended to 0.1–10 pc-scale (Bally 2016). Expanding bubbles of 1–10 pc generated by stellar winds from intermediate-mass and high-mass stars have been discovered in nearby clouds (Arce et al. 2011; Feddersen et al. 2018; Pabst et al. 2019). Far-ultraviolet (FUV) radiation from high-mass stars sometimes affects the parent clouds at 10 pc scale (Shimajiri et al. 2011; Ishii et al. 2019). Much larger bubbles created by supernovae interact with entire molecular clouds (Frisch et al. 2015). Galactic spiral density waves influence molecular cloud formation and subsequent star formation (Elmegreen 1979). One of the immediate objectives of the present project is to reveal cloud structures and the dynamics of target clouds to attempt to elucidate how such events influence them. In summary, wide-field mapping observations are important to understand the effects of stellar feedback and external events like large-scale shocks because they potentially affect cloud properties and structures at a cloud scale, 1–10 pc. For comparison, we summarize several recent wide-field surveys toward our target clouds in table 1. For Orion A, many molecular-line mapping surveys have been done to date, but many of these surveys were observed only in the northern parts including OMC-1. For the Aquila Rift, many molecular-line mapping surveys have just focused on the two prominent star-forming regions, W 40 and Serpens South. As for M 17, only a few wide-field surveys that cover at least about a  $1 \text{ deg}^2$  area have been done so far.

The main objectives of the present paper are to give a project overview and to describe the details of the observations and calibration of the obtained data. In section 2 we describe how we select our target clouds and lines.

**Table 1.** Selected recent wide-field surveys toward Orion A, Aquila Rift, and M 17.\*

Telescope/survey	Line/continuum	Resolution	Cloud/key reference
Osaka Pref. 1.85 m	$^{12}\text{CO}/^{13}\text{CO}/\text{C}^{18}\text{O } J = 2-1$	2'7	Orion A/Nishimura et al. (2015)
Tsukuba 30 cm	$^{12}\text{CO } J = 4-3$	9'4	Orion A/Ishii et al. (2016)
Harvard-CfA 1.2 m	$^{12}\text{CO } J = 1-0$	8'4	Orion A/Wilson et al. (2005)
ASTE, NRO 45 m	1.1 m/ $^{12}\text{CO } J = 1-0$	36''/21''	Orion A/Shimajiri et al. (2011)
JCMT/GBS	$^{13}\text{CO}/\text{C}^{18}\text{O } J = 3-2$	17''	Orion A/Buckle et al. (2012)
FCRAO 14 m	$^{12}\text{CO}/^{13}\text{CO } J = 1-0$	46''	Orion A/Ripple et al. (2013)
IRAM 30 m	$^{12}\text{CO}/^{13}\text{CO } J = 2-1$	11''	Orion A/Berné, Marcelino, and Cernicharo (2014)
ASTE 10 m	$^{12}\text{CO } J = 3-2$	30''	Orion A/Takahashi et al. (2008)
Herschel/HIFI	$\text{CH}^+/\text{CO } (J = 10-9)/\text{HCN/}$	12''-27''	Orion A (OMC-1)/Goicoechea et al. (2019)
IRAM 30 m	$\text{HCO}^+ (J = 6-5), \dots$		
Herschel-Planck	dust continuum	36''	Orion A/Lombardi et al. (2014)
Spitzer	MIR 3-24 $\mu\text{m}$	2''-5''	Orion A/Megeath et al. (2012)
VISTA/VISION	NIR 0.85-2.4 $\mu\text{m}$	0''85	Orion A/Meingast et al. (2016)
IN-SYNC	NIR 1.5-1.6 $\mu\text{m}$	1''6	Orion A/Da Rio et al. (2016)
NRO 45 m	$\text{N}_2\text{H}^+ J = 1-0$	21''	Orion A/Tatematsu et al. (2008)
NRO 45 m	$\text{H}^{13}\text{CO}^+ J = 1-0$	21''	Orion A/Ikeda, Sunada, and Kitamura (2007)
CARMA + NRO 45 m/CARMA-NRO	$^{12}\text{CO}/^{13}\text{CO}/\text{C}^{18}\text{O } J = 1-0$	8''	Orion A/Kong et al. (2018)
Orion			
NRO 45 m	$^{12}\text{CO}/^{13}\text{CO}/\text{C}^{18}\text{O}/\text{N}_2\text{H}^+ J = 1-0/\text{CCS}$ $J_N = 7_6-6_5$	21''-24''	Orion A/this paper
Harvard-CfA 1.2 m	$^{12}\text{CO } J = 1-0$	8'4	Aquila/Dame Hartmann, and Thaddeus (2001)
Osaka pref. 1.85 m	$^{12}\text{CO}/^{13}\text{CO}/\text{C}^{18}\text{O } J = 2-1$	2'7	Aquila/Nakamura et al. (2017)
Herschel	dust	36''	Aquila/André et al. (2010)
IRAM 30 m/MAMBO	1.2 mm	11''	Aquila/Maury et al. (2011)
IRAM 30 m	$\text{HCN}/\text{H}^{13}\text{CN}/\text{HCO}^+/\text{H}^{13}\text{CO}^+ J = 1-0$	40''	Aquila/Shimajiri et al. (2017)
JCMT/GBS	850 $\mu\text{m } ^{12}\text{CO } J = 3-2$	15''/22''	Aquila (W 40)/Rumble et al. (2016)
ASTE 10 m	$^{12}\text{CO } J = 3-2/\text{HCO}^+ J = 4-3$	31''	Aquila (W 40)/Shimoikura et al. (2015)
ASTE 10 m	$^{12}\text{CO } J = 3-2/\text{HCO}^+ J = 4-3$	24''	Aquila (Serpens South)/Nakamura et al. (2011b)
Spitzer	IRAC	2''	Aquila (Serpens South)/Gutermuth et al. (2008)
NRO 45 m	$\text{N}_2\text{H}^+ J = 1-0$	24''	Aquila (Serpens South)/Tanaka et al. (2013)
MOPRA	$\text{N}_2\text{H}^+/\text{H}^{13}\text{CN}/\text{HCN/}$ $\text{HNC}/\text{HCO}^+/\text{H}^{13}\text{CO}^+ J = 1-0$	40''	Aquila (Serpens South)/Kirk et al. (2013)
NRO 45 m	$\text{CCS } J_N = 4_3-3_2/\text{HC}_3\text{N } J = 5-4$	37''	Aquila (Serpens South)/Nakamura et al. (2014)
NRO 45 m	$^{12}\text{CO}/^{13}\text{CO}/\text{C}^{18}\text{O}/\text{N}_2\text{H}^+ J = 1-0/\text{CCS}$ $J_N = 7_6-6_5$	21''-24''	Aquila/this paper
Spitzer	MIR	2''	M 17/Povich & Whitney (2010); Povich et al. (2016)
HHT 10 m	$^{12}\text{CO}/^{13}\text{CO } J = 2-1$	32''	M 17/Povich et al. (2009)
NRO 45 m	$^{12}\text{CO}/^{13}\text{CO}/\text{C}^{18}\text{O } J = 1-0$	20''	M 17/Nishimura et al. (2018)
NRO 45 m	$^{12}\text{CO}/^{13}\text{CO}/\text{C}^{18}\text{O}/\text{N}_2\text{H}^+ J = 1-0/\text{CCS}$ $J_N = 7_6-6_5$	21''-24''	M 17/this paper

\*This is not a complete list of the recent wide-field survey. See also table 1 of Kong et al. (2018) for Orion A.

The details of the observations are described in section 3. In section 4 we describe how to produce the final data cubes. Then we summarize the quality of our maps in terms of sensitivity, angular resolution, and velocity resolution. In section 5 we present the spatial distributions of the molecular line emissions obtained, and in section 6 we derive the spatial distribution of the  $^{13}\text{CO}$  and  $\text{C}^{18}\text{O}$  abundances toward Orion A. We briefly discuss the global molecular gas distributions of the target clouds mainly using  $^{12}\text{CO}$  and its

isotopologues. In section 7 we show the preliminary results of a CO outflow survey toward L 1641 N in Orion A and Serpens South in the Aquila Rift, demonstrating that our data can be used to detect outflows. Finally, we summarize the main results in section 8.

The detailed analysis will be presented in separate papers. For example, Tanabe et al. (2019), Ishii et al. (2019), and Nakamura et al. (2019) describe the results of the outflow survey, cloud structure analysis, and

**Table 2.** Spatial resolutions achieved for the Nobeyama 45 m, CARMA, and ALMA observations.\*

Telescopes	Angular resolution	Nearest regions ~140 pc (Taurus, $\rho$ Oph)	Intermediate regions ~400 pc (Orion A, Aquila Rift, California)	Distant regions ~3 kpc (M 17, several IRDCs <sup>†</sup> )
NRO 45 m only	~20''	2800 au (0.014 pc)	8400 au (0.04 pc)	40000 au (0.2 pc)
CARMA + NRO 45 m	~8''	—	3300 au	—
ALMA	~1''	140 au	420 au	3000 au

\*The distances are adopted from the following references: nearest regions—Taurus (137 pc; Torres et al. 2007; Loinard et al. 2007),  $\rho$  Oph (137 pc; Ortiz-León et al. 2017a); intermediate regions—Orion A (414 pc; Menten et al. 2007; Kim et al. 2008), Aquila Rift (436 pc, Ortiz-León et al. 2017b); distant regions—M 17 (2.0 kpc; Xu et al. 2011). The star-forming regions indicated by boldface are the target clouds of the present project. We note that for the M 17 region, several clouds with different distances seem to be overlapped along the line of sight (Povich et al. 2016). Here we refer to the ALMA observations just for comparison of the spatial resolutions achieved. In the present paper, we present the data obtained with the Nobeyama 45 m telescope. The detail of the CARMA + Nobeyama combined data is presented in Kong et al. (2018).

<sup>†</sup>Infrared dark clouds.

multi-line observations of the OMC-2 FIR 4 region for Orion A, respectively. Shimoikura et al. (2019b) and Kusune et al. (2019) present the detailed cloud kinematic structure and the relationship between filamentary structure and magnetic field, respectively, toward Aquila Rift. For M 17, Nguyen Luong et al. (2019), Shimoikura et al. (2019a), and Sugitani et al. (2019) will report the global cloud kinematics, dense core survey, and relationship between cloud structure and magnetic field, respectively. In addition to the three main regions, a few other star-forming regions such as the Northern Coal Sack (Dobashi et al. 2019a) and DR 21 (Dobashi et al. 2019b) were studied during our project. These data were obtained for intensity calibration of the CO lines taken with a new 100 GHz receiver, FOREST.

## 2 Project overview

### 2.1 Molecular line data with a $10^{-2}$ pc resolution within distances of a few kpc

In 2011, the state-of-art facility ALMA started science operations. Since then, we can easily conduct observations with much higher sensitivity and higher angular resolution than ever done before. In the ALMA era, one of the important objectives of our project is to make useful datasets to compare with ALMA maps of distant molecular clouds. Even using one of the largest millimeter telescopes, the Nobeyama 45 m telescope, the achieved beam size at 115 GHz is at most ~15''. On the other hand, we can easily achieve ~1'' resolution using ALMA. To overcome the disadvantage of the coarse angular resolution, we choose nearby molecular clouds as our targets for the Nobeyama 45 m telescope. Large-scale ALMA mapping observations toward nearby molecular clouds are still limited and are impossible to do because of its small field of view and extremely long observation time. On the other hand, the coarse beams of single-dish telescopes allow us

to conduct wide-field mapping observations. In this sense, our Nobeyama mapping project is complementary to the ALMA observations toward distant molecular clouds.

Previous observational studies have often been influenced by the effects of different *spatial* resolutions when cloud structure and physical properties of molecular clouds are compared. We would like to minimize the effects of the different spatial resolution to better understand the cloud structure and the environmental effects. In our project we therefore aim to obtain maps that can be compared directly with those obtained with ALMA in almost the same *spatial* resolution.

The number of pointings of the ALMA mosaic observations is limited to below 150 for the 12 m array, which can cover an area of  $\lesssim 5' \times 5'$  with an angular resolution of 1'' in the ALMA band-3 (~100 GHz). Assuming that we map about 1 deg<sup>2</sup> area with an angular resolution of 20'' toward regions whose distances are 20 times closer than the areas observed by ALMA with 1'' resolution, both the maps obtained have comparable spatial coverage and spatial resolution. As described below, we thus chose Orion A, Aquila Rift, and M 17 as our targets for the Nobeyama 45 m mapping observations. In table 2 we compare the achieved spatial resolutions for several molecular clouds, mainly including our target regions. In our previous Nobeyama 45 m observations we have mapped the nearest molecular clouds (~140 pc) such as L 1551 (Yoshida et al. 2010; Lin et al. 2017) and the  $\rho$  Ophiuchus cloud (Maruta et al. 2010; Nakamura et al. 2011a) using the Nobeyama 45 m telescope. These maps have a spatial resolution of about 2000–3000 au, which is comparable to those of the maps of Orion A (414 pc) combined with the CARMA data (Kong et al. 2018). For more distant clouds with distances of a few kpc, ALMA observations can achieve a spatial resolution of a few thousand au at an angular resolution of ~1''. Thus, our Nobeyama maps of nearby clouds can be directly compared with the maps of the molecular clouds

**Table 3.** Observed lines.\*

Molecule	Transition	Rest frequency (GHz)	Beam size ( $''$ )	$\Delta V$ ( $\text{km s}^{-1}$ )	Main beam efficiency ( $\eta$ )
$^{12}\text{CO}$	$J = 1-0$	115.271204	$14.3 \pm 0.4$	0.1	$41.6 \pm 3\%$
$^{13}\text{CO}$	$J = 1-0$	110.201354	$14.9 \pm 0.4$	0.1	$43.5 \pm 3\%$
$\text{C}^{18}\text{O}$	$J = 1-0$	109.782176	$14.9 \pm 0.4$	0.1	$43.7 \pm 3\%$
$\text{N}_2\text{H}^+$	$J = 1-0$	93.1737637	$17 \pm 0.5$	0.1	$50.0 \pm 5\%$
CCS	$J_N = 8_7-7_6$	93.870098	$17 \pm 0.5$	0.1	$49.7 \pm 5\%$

\*The rest frequency of the main hyperfine component of  $\text{N}_2\text{H}^+$  is adopted from Pagani, Daniel, and Dubernet (2009). The beam size and main beam efficiencies listed are those measured with FOREST. The errors in the efficiencies are mainly due to the uncertainty of the brightness temperature of the planets used for the measurements. See the NRO web page for more details.

within a few kpc in a comparable spatial resolution of a few thousand au.

We have opened all the mapping data we took in this project to the public. The data are available through the Japanese Virtual Observatory (JVO) archival system.<sup>1</sup>

## 2.2 Target lines

We chose the following five molecular lines:  $^{12}\text{CO}$  ( $J = 1-0$ ),  $^{13}\text{CO}$  ( $J = 1-0$ ),  $\text{C}^{18}\text{O}$  ( $J = 1-0$ ),  $\text{N}_2\text{H}^+$  ( $J = 1-0$ ), and CCS ( $J_N = 8_7-7_6$ ). The  $^{12}\text{CO}$  molecule is the second most abundant after the hydrogen molecule in molecular clouds, and therefore it can trace the basic cloud structure reasonably well. Rarer isotopologues of  $^{12}\text{CO}$  such as  $^{13}\text{CO}$  and  $\text{C}^{18}\text{O}$  can trace relatively denser gas with densities of  $10^3$ – $10^4 \text{ cm}^{-3}$ .  $\text{N}_2\text{H}^+$  has a critical density of  $\sim 10^5 \text{ cm}^{-3}$  and traces cold dense gas, particularly in the prestellar phase, very well (Caselli et al. 2002; Punanova et al. 2016). Thus, we can cover the densities from  $10^2 \text{ cm}^{-3}$  to  $10^6 \text{ cm}^{-3}$  using these four lines. The main reason for choosing CCS is that it can be obtained simultaneously with  $^{13}\text{CO}$  ( $J = 1-0$ ),  $\text{C}^{18}\text{O}$  ( $J = 1-0$ ), and  $\text{N}_2\text{H}^+$  ( $J = 1-0$ ), as we mention below. CCS is abundant in the early prestellar phase and traces a similar density range to  $\text{N}_2\text{H}^+$ . Thus, CCS can provide additional information on the chemical evolution of prestellar dense gas (Suzuki et al. 1992; Marka et al. 2012; Loison et al. 2014; Shimoikura et al. 2018).

Another reason why we mainly chose the CO lines is that the main beam efficiencies of the 45 m telescope in the 100 GHz band ( $\lesssim 0.5$ ) are not as superb as those of other telescopes such as the IRAM 30 m and LMT telescopes (see table 3) and thus observations of strong emission lines such as  $^{12}\text{CO}$  and its isotopologues can be done more efficiently within a limited observation time. Although  $\text{N}_2\text{H}^+$  is not as strong as  $^{12}\text{CO}$ ,  $^{13}\text{CO}$ , or  $\text{C}^{18}\text{O}$ , a new multi-beam superconductor–insulator–superconductor (SIS) receiver, FOREST, allows us to observe  $\text{N}_2\text{H}^+$  line simultaneously with  $^{13}\text{CO}$  and  $\text{C}^{18}\text{O}$ . In addition, CCS ( $J_N = 8_7-7_6$ ) can

also be obtained simultaneously with  $\text{N}_2\text{H}^+$ ,  $^{13}\text{CO}$ , and  $\text{C}^{18}\text{O}$  using a spectral window mode that has become available since the 2016–2017 season.

We also adopted a velocity resolution of  $\sim 0.1 \text{ km s}^{-1}$ , so that we can reasonably identify dense cores with a typical internal velocity dispersion of a few tenths  $\text{km s}^{-1}$ . Our observed emission lines are summarized in table 3.

## 2.3 Target clouds

We chose the target clouds taking into account the following conditions:

- (1) The main part of the target cloud can be covered by  $1 \text{ deg}^2$  with a few hundred hours using the new 100 GHz four-beam SIS receiver FOREST, including overhead such as pointing observations and flux calibration.
- (2) The target clouds are relatively well studied, and additional datasets are available.
- (3) Each target cloud contains regions of ongoing high-mass star formation.
- (4) The spatial resolution of the Nobeyama 45 m data can be comparable to or smaller than the typical size of dense cores ( $\sim 0.1 \text{ pc}$ ).

Taking the above conditions into account, we chose the following three regions as our targets: (1) Orion A ( $d \sim 414 \text{ pc}$ ; Menten et al. 2007; Kim et al. 2008), (2) Aquila Rift ( $d \sim 436 \text{ pc}$ ; Ortiz-León et al. 2017b), and (3) M17 ( $d \sim 2000 \text{ pc}$ ; Xu et al. 2011).

In this survey we chose nearby clouds that contain the formation sites of O-type and early B-type stars. There are not so many such regions within  $\sim 1 \text{ kpc}$  (e.g., Orion A, Aquila Rift, California, Mon R2, and Orion B). Among them, Orion A and the Aquila Rift may be the nearest. The evolutionary stages of the star-forming regions appear to be different in the Aquila Rift and Orion A. For example, star formation lasts at least a few Myr in OMC-1 (Da Rio et al. 2016). On the other hand, in the Serpens South cluster in the Aquila Rift, the fraction of Class O/I protostars is extremely high, suggesting an age within 0.5 Myr. In other

<sup>1</sup> (<http://jvo.nao.ac.jp/index-e.html>).

words, Orion A contains more evolved star-forming regions than the Aquila Rift. The distances of Orion A and the Aquila Rift are similar ( $\sim 400$  pc), and thus it is easy to directly compare the cloud structures with the same spatial resolutions for molecular clouds in different evolutionary stages. These are the main reason why we chose these two clouds. The star formation efficiencies of Orion A and the Aquila Rift appear to be similar within a few percent of each other (Evans 2009; Maury et al. 2011), which is typical of nearby star-forming regions (Krumholz & Tan 2007). Thus, we believe that the two regions are representative of nearby star-forming molecular clouds.

The beam size of the Nobeyama 45 m telescope at 100 GHz is  $\sim 15''$ , corresponding to  $\sim 6200$  au and 30000 au at the distances of 414 pc and 2000 pc, respectively. The spatial resolution of M 17 is not satisfied with the last condition, but we chose it for the following two reasons.

- The densest part of an infrared dark cloud in M 17, M 17 SWex, was observed by ALMA, and the  $\text{N}_2\text{H}^+$  data are available (see, e.g., Ohashi et al. 2016; Chen et al. 2019), and we can combine the 45 m data with the ALMA data to fill the zero spacing so that we can make maps whose spatial resolution is comparable to the other two targets obtained with the Nobeyama 45 m telescope ( $\sim 8000$  au).
- Star formation activity in M 17 appears to be triggered by a Galactic spiral wave passage (Elmegreen 1979) and thus the M 17 data are expected to provide us with a clue to better understand the Galactic star formation process. In addition, M 17 is the nearest high-mass star-forming region to the Sagittarius arm. The stellar density at NGC 6811 is the highest at  $>10^3$  star pc $^{-2}$  after the Carina cluster among the regions in the MYStIX survey of massive star-forming regions in X-ray (Kuhn et al. 2015). M 17 is closer to us than the Carina region. Povich and Whitney (2010) proposed that high mass star formation may be delayed in an IRDC region and the mass function of young stars in IRDCs appears to be different from the Salpeter initial mass function. M 17 is expected to provide us with key information to understand how high-mass stars form. Therefore, we chose the distant high-mass star-forming region M 17.

For Orion A, we combine our Nobeyama 45 m data with the CARMA interferometric data to obtain maps with  $\sim 8''$  resolution. The combined maps have *spatial* resolution comparable to those of the Taurus and  $\rho$  Ophiuchus molecular clouds previously obtained with the Nobeyama 45 m telescope, with a spatial resolution of about 3000 au ( $\sim 20''$ ) at a distance of 140 pc. Thus, using the Nobeyama data and ALMA data, we can directly compare the internal structure and physical properties of several clouds located

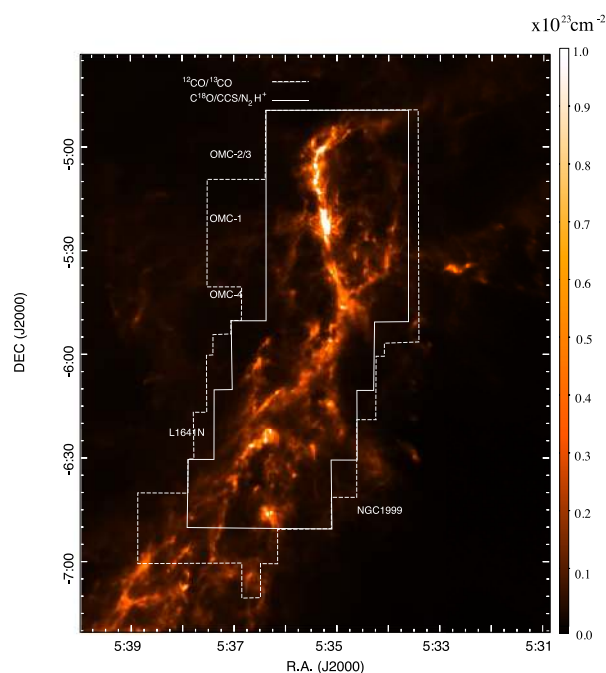


**Fig. 1.** Observation areas overlaid on the  $\text{H}_2$  column density maps of Orion A. The solid and dashed lines indicate the observation boxes for the  $^{12}\text{CO}+^{13}\text{CO}$  set and the  $\text{C}^{18}\text{O}+\text{N}_2\text{H}^++\text{CCS}$  set, respectively. The  $\text{H}_2$  column density map has an effective angular resolution of about  $\sim 36''$  (see Lombardi et al. 2014). (Color online)

at different distances in the range from 140 pc to a few kpc with the same *spatial* resolutions (see table 2). We expect that the maps obtained will be useful as templates for nearby molecular clouds that can be compared with maps toward more distant molecular clouds, which can be obtained with ALMA, e.g., IRDCs at a few kpc such as the Nessie nebula and G11.11–0.12 (Snake).

We determine the mapping areas by reference to the 2MASS  $A_V$  maps (Dobashi et al. 2005; Dobashi 2011), Herschel column density maps, and Spitzer images. Taking the observation time into account, we planned to map the target areas with  $A_V \gtrsim$  a few mag corresponding to a few tenths g cm $^{-2}$ , so that we can detect almost all the self-gravitating cores in our target clouds—see the  $A_V$  threshold derived by André et al. (2010).

Figures 1, 2, and 3 present the mapping areas of Orion A, Aquila Rift, and M 17, respectively, overlaid on the Herschel or Spitzer images.

### 3 Observations

As described in the next section, we used the molecular line data taken with BEARS for intensity calibration. In this section we first describe the details of the FOREST observations, and then describe the details of the BEARS observations. BEARS is an SIS 25-element focal plane receiver with

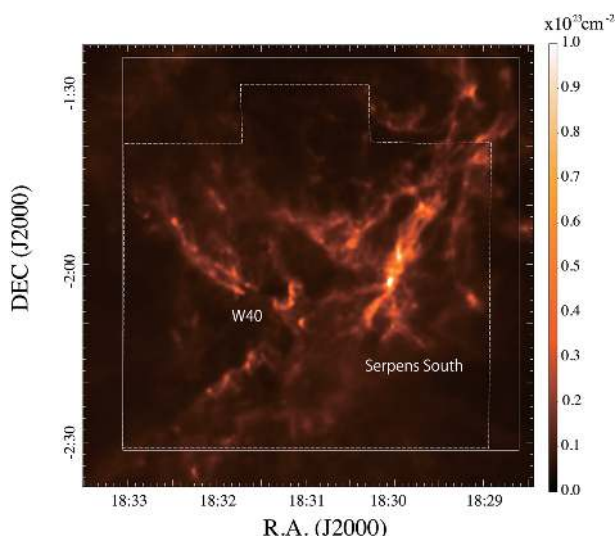


**Fig. 2.** Same as figure 1 but for the Aquila Rift. The color image shows the  $\text{H}_2$  column density map whose fitting data were downloaded via the Herschel Gould Belt Survey Archive system. The solid and dashed lines are the same as those in figure 1. (Color online)

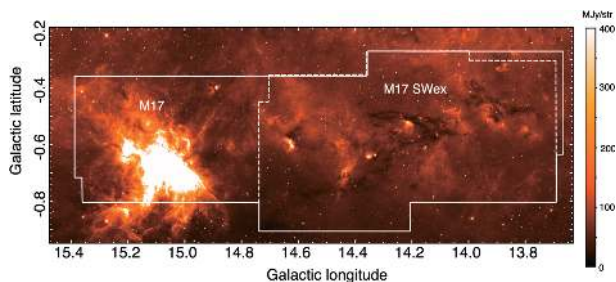


**Fig. 3.** Observation areas overlaid on the Spitzer  $8\mu\text{m}$  image of M17. The color image shows the Spitzer  $8\mu\text{m}$  image of M17 downloaded from the Glimpse Archival system. The solid and dashed lines are the same as those in figure 1. (Color online)

a frequency coverage of 82–116 GHz, and has been used for many mapping observations since 2000. Therefore, the intensity calibration scheme is well established compared to the new receiver, FOREST, which was also demounted for repair after the first season and reinstalled in the second season. In addition, the surface accuracy of the telescope dish was significantly improved for the first two seasons by applying a holograph to the dish surface. Careful data reduction of the data obtained is crucial to verify the absolute intensity scale of the FOREST data. Thus, we used the data taken with BEARS for intensity calibration. For both observations we adopted the on-the-fly (OTF) mapping mode with a position-switching method using the emission-free positions areas summarized in table 6.

For FOREST, we adopted two frequency sets to observe the target lines. Set 1 is for  $^{12}\text{CO}$  and  $^{13}\text{CO}$ , while set 2 is for  $\text{C}^{18}\text{O}$ ,  $\text{N}_2\text{H}^+$ ,  $^{13}\text{CO}$ , and CCS with a spectral window

**Table 4.** Sizes of observation boxes for the FOREST observations.\*

Lines	Scan	$^{12}\text{CO}/^{13}\text{CO}$	$\text{C}^{18}\text{O}/\text{N}_2\text{H}^+$	$^{13}\text{CO}/\text{C}^{18}\text{O}/\text{N}_2\text{H}^+/\text{CCS}$
Season		2014–2015/2015–2016/2016–2017	2015–2016	2016–2017
Orion A	x	$10' \times 5'$	$20' \times 5'$	$20' \times 5'$
Orion A	y	$5' \times 10'$	$5' \times 20'$	$5' \times 20'$
Aquila Rift	x	$20' \times 10'$	—	$20' \times 10'$
Aquila Rift	y	$10' \times 20'$	—	—
M17	x	$20' \times 10'$	$20' \times 10'$	$20' \times 10'$
M17	y	$10' \times 20'$	$10' \times 20'$	$10' \times 20'$

\*Taking into account the observation schedule of each season, we changed the observation box sizes. For Aquila Rift, we could not obtain y-scan data of  $\text{C}^{18}\text{O}$ ,  $\text{N}_2\text{H}^+$ , or CCS. In addition, for M17, we significantly reduced the observation area for the  $\text{C}^{18}\text{O}$ ,  $\text{N}_2\text{H}^+$ , and CCS observations. These incomplete observations are mainly due to a malfunction of the master collimeter driving system that happened in the 2016–2017 season.

**Table 5.** Parameters of observations with FOREST.\*

Box size	$10' \times 5'$	$20' \times 5'$	$20' \times 10'$
Time for scan (s)	15	30	26
Number of ONs per OFF	4	2	3
Separation between scans	$5''17$	$5''17$	$5''17$
Frequency resolution (kHz)	15.26	15.26	15.26

\*For all observations, scans of the OTF observations are separated in intervals of  $5''17$ . Thus, individual scans by the four beams of FOREST are completely overlapped. This greatly minimizes the effort needed for flux calibration.

mode. For BEARS, we observed only a single line for the individual observations.

### 3.1 FOREST

FOREST is a four-beam dual-polarization sideband-separating SIS receiver (Minamidani et al. 2016) and has 16 intermediate frequency (IF) outputs in total; 8 IFs in the upper-sideband and the other 8 IFs in the lower-sideband were used for the molecular line observations. As backends, we used a digital spectrometer based on an FX-type correlator, SAM45, that has 16 sets of 4096 channel arrays. We divided the mapping area into smaller sub-areas whose sizes are summarized in table 4. Then, we carried out OTF observations toward each sub-area. The parameters of the OTF observations are summarized in table 5. Scans of the OTF observations were separated in intervals of  $5''17$ . Thus, individual scans of the four beams of FOREST are overlapped. The positions of the emission-free areas used for the observations are summarized in table 6. We note that the coordinates of the emission-free areas are those of the first FOREST beam.

**Table 6.** Map coverage and positions of emission-free areas used for the observations and SiO maser objects used for the pointing observations.\*

Regions	Map coverage	Emission-free areas		Pointing objects (SiO maser line)		
		RA (J2000.0)	Dec (J2000.0)	RA (J2000.0)	Dec (J2000.0)	
Orion A	0°7' × 2°	05 <sup>h</sup> 29 <sup>m</sup> 00 <sup>s</sup> .0	−05°25'30"0	05 <sup>h</sup> 35 <sup>m</sup> 14 <sup>s</sup> .16	−05°22'21"5	Orion KL
Aquila Rift	1° × 1°	18 <sup>h</sup> 41 <sup>m</sup> 19 <sup>s</sup> .09	+04°12'00"0	18 <sup>h</sup> 37 <sup>m</sup> 19 <sup>s</sup> .26	+10°25'42"2	V1111-Oph
M17	2° × 0°5'	18 <sup>h</sup> 37 <sup>m</sup> 19 <sup>s</sup> .26	+10°25'42"2	18 <sup>h</sup> 37 <sup>m</sup> 19 <sup>s</sup> .26	+10°25'42"2	V1111-Oph

\*These areas and objects were used for both the BEARS and FOREST observations.

**Table 7.** Summary of the FOREST observations.

Lines	Period	Observation time	$T_{\text{sys}}^*$	Velocity resolution	Noise level
Orion A					
<sup>12</sup> CO	2014 Dec–2016 Dec	150 hr	350–400 K	0.1 km s <sup>−1</sup>	0.50–1.5 K
<sup>13</sup> CO	2014 Dec–2017 Mar	150 hr	150–200 K	0.1 km s <sup>−1</sup>	0.20–0.30 K
C <sup>18</sup> O	2017 Jan–2017 Mar	150 hr	150–200 K	0.1 km s <sup>−1</sup>	0.26–0.30 K
CCS	2017 Jan–2017 Mar	150 hr	150–200 K	0.1 km s <sup>−1</sup>	0.30–0.49 K
N <sub>2</sub> H <sup>+</sup>	2017 Jan–2017 Mar	150 hr	150–200 K	0.1 km s <sup>−1</sup>	0.26–0.30 K
Aquila Rift					
<sup>12</sup> CO	2015 Mar–2017 Mar	50 hr	300–500 K	0.1 km s <sup>−1</sup>	0.38–0.50 K
<sup>13</sup> CO	2015 Mar–2017 Mar	150 hr	150–200 K	0.1 km s <sup>−1</sup>	0.38–0.50 K
C <sup>18</sup> O	2016 Mar–2017 Mar	120 hr	150–200 K	0.1 km s <sup>−1</sup>	0.20–0.30 K
CCS	2016 Mar–2017 Mar	120 hr	150–200 K	0.1 km s <sup>−1</sup>	0.17–0.20 K
N <sub>2</sub> H <sup>+</sup>	2016 Mar–2017 Mar	120 hr	150–200 K	0.1 km s <sup>−1</sup>	0.18–0.22 K
M17					
<sup>12</sup> CO	2015 Mar–2017 Mar	25 hr	300–500 K	0.1 km s <sup>−1</sup>	0.48–1.7 K
<sup>13</sup> CO	2015 Mar–2017 Mar	150 hr	150–200 K	0.1 km s <sup>−1</sup>	0.16–0.80 K
C <sup>18</sup> O	2016 Mar–2017 Mar	65 hr	150–200 K	0.1 km s <sup>−1</sup>	0.17–0.34 K
CCS	2016 Mar–2017 Mar	65 hr	150–200 K	0.1 km s <sup>−1</sup>	0.20–0.27 K
N <sub>2</sub> H <sup>+</sup>	2016 Mar–2017 Mar	65 hr	150–200 K	0.1 km s <sup>−1</sup>	0.15–0.27 K

\*The values of  $T_{\text{sys}}$  are given in the single sideband.

Calibration of the observations was done by the chopper wheel technique to convert the output signal into the antenna temperature  $T_A^*$ , corrected for atmospheric attenuation. Some details of the observations are also summarized in table 7. The telescope pointing was checked every 1 hr by observing the SiO maser lines from the objects presented in table 6. The pointing accuracy was better than  $\sim 3''$  throughout the entire observation.

In order to minimize the scanning effects, data with orthogonal scanning directions along the RA and Dec. axes were combined into a single map. We adopted the same gridding convolution function (spheroidal function) as the BEARS data to calculate the intensity at each grid point of the final cube data with a spatial grid size of  $7''.5$ .

The FOREST receiver and telescope conditions were not stable for the first two seasons. For example, the receiver was demounted in 2016 June (right after the first season) to improve several internal components. Second, the surface

accuracy of the 45 m dish was significantly improved for the first two seasons by applying a holograph to the dish surface. Therefore, the observation conditions were different from season to season. To minimize the effects of these factors in determining the intensity scale of the observed lines, we scaled the data obtained with FOREST by those of BEARS whose intensity calibration method is well established. The detail of the flux calibration of the FOREST data is described in the next section.

In the last season (2016–2017), a new observational capability called a spectral window mode was available, which allows us to obtain more lines simultaneously. We therefore observed <sup>13</sup>CO ( $J = 1-0$ ), C<sup>18</sup>O ( $J = 1-0$ ), N<sub>2</sub>H<sup>+</sup> ( $J = 1-0$ ), and CCS ( $J_N = 7_6-6_5$ ) simultaneously. In the spectral window mode, we equally divided the whole bandwidth into two, so that the bandwidth and frequency resolution of the spectrometer arrays were set to 31.25 MHz and 15.26 kHz, respectively.



**Table 8.** Summary of the BEARS observations.

Lines	Period	Observation time	$T_{\text{sys}}^*$	Velocity resolution	Noise level	Observation mode	Ref. <sup>†</sup>
Orion A							
<sup>12</sup> CO (north)	2007 Dec–2008 May	~40 hr	250–500 K	0.2 km s <sup>-1</sup>	0.4 K	OTF	1
<sup>12</sup> CO (south)	2009 Dec–2010 Jan	~20 hr	300–600 K	0.5 km s <sup>-1</sup>	0.52 K	OTF	2
<sup>13</sup> CO (north)	2013 May	~50 hr	270–470 K	0.3 km s <sup>-1</sup>	0.7 K	OTF	3
<sup>13</sup> CO (south)	2012 Apr–2013 Mar	~60 hr	210–400 K	0.1 km s <sup>-1</sup>	1.96 K	OTF	4
C <sup>18</sup> O (north)	2010 Mar–2013 May	~100 hr	270–470 K	0.1 km s <sup>-1</sup>	0.3 K	OTF	3
Aquila Rift (Serpens South)							
<sup>12</sup> CO	2011 Apr–2011 May	~15 hr	250–500 K	0.5 km s <sup>-1</sup>	1.3 K	OTF	4
<sup>13</sup> CO	2011 Apr–2011 May	~30 hr	210–400 K	0.5 km s <sup>-1</sup>	0.88 K	OTF	4
C <sup>18</sup> O	2011 Apr–2014 Apr	~30 hr	200–400 K	0.1 km s <sup>-1</sup>	0.9 K	OTF	4

\*The values of  $T_{\text{sys}}$  are given in the double sideband.

<sup>†</sup>References. 1: Shimajiri et al. (2011); 2: Nakamura et al. (2012); 3: Shimajiri et al. (2014); 4: This paper.

### 3.2 BEARS

The procedure for the BEARS observations was basically similar to that of FOREST. The details of the BEARS observations are summarized in table 8. Some of the results of the BEARS observations are described in the references listed in the last column of table 8. In brief, we divided the mapping area into many 15' × 15' or 20' × 20' rectangle sub-areas. The sizes of these sub-areas were determined so as to complete an OTF scan within 1 or 1.5 hr. We carried out mapping observations toward each sub-region in OTF mode (Sawada et al. 2008) using BEARS and 25 sets of 1024 channel auto correlators (ACs) which have a bandwidth of 32 MHz and frequency resolution of 37.8 kHz. The velocity resolutions of the observations for individual lines are listed in table 8.

Calibration of the observations was done by the chopper wheel technique to convert the output signal into the antenna temperature  $T_A^*$ , corrected for atmospheric attenuation. At 110 GHz, the half-power beam width was about 15'', which corresponds to about 0.03 pc at a distance of 414 pc. The main beam efficiency ( $\eta_{45\text{ m}}$ ) was about 0.5 at 110 GHz for the corresponding observation season. The telescope pointing was checked every 1 or 1.5 hr by observing the SiO maser sources Orion KL and IRC +00363 for the Orion A and Serpens South observations, respectively, and was better than 3'' during the whole observing period.

We obtained a map by combining scans along two axes that run at right angles to each other. We adopted a convolutional scheme with a spheroidal function to calculate the intensity at each grid point of the final cube data with a grid size of 7''.5. This convolutional scheme is the same as that of the FOREST data. The spheroidal function is given by Sawada et al. (2008). The resulting effective resolution

was about 21'' at 110 GHz. Finally, we converted the intensities in the antenna temperature scale ( $T_A^*$ ) into those in the brightness temperature scale ( $T_{\text{mb}}$ ) by dividing by the main beam efficiencies ( $\eta$ ),  $T_{\text{mb}} = T_A^*/\eta$ . The typical rms noise levels of the final maps are listed in table 8. We note that for Orion A, the coverages of the <sup>12</sup>CO and <sup>13</sup>CO maps taken with BEARS are from Dec  $\sim -5^\circ 20'$  to  $\sim -6^\circ 30'$ , which is slightly smaller than the actual mapping area of the FOREST observations. The coverage of the C<sup>18</sup>O map was much smaller than those of <sup>12</sup>CO and <sup>13</sup>CO. For the other lines (N<sub>2</sub>H<sup>+</sup> and CCS), no OTF data were available. The typical noise levels achieved for the BEARS observations were  $\sim 0.4$  K and  $0.7$  K at  $0.1$  km s<sup>-1</sup> for <sup>12</sup>CO and <sup>13</sup>CO, respectively.

### 4 Flux calibration

The procedure of flux calibration is complicated, as we describe in this section. First, we briefly summarize our flux calibration procedure, and then we describe the details of the procedure in the subsequent subsections.

0. All the data were converted to intensity data in  $T_A^*$  using the standard NRO data reduction tool, NOSTAR.
1. For the <sup>12</sup>CO and <sup>13</sup>CO observations of Orion A, the intensities of each emission line and each sub-box were multiplied by the scaling factor  $SF_i^{\text{BEARS},l}$ , where the scaling factor  $SF_i^{\text{BEARS},l}$  is the ratio of the integrated intensity of the FOREST observations to that obtained with BEARS for the corresponding sub-box  $i$ ; the superscript  $l$  indicates the corresponding line (<sup>12</sup>CO or <sup>13</sup>CO). For the sub-boxes where BEARS data were not available, the average scaling factor of the corresponding season is adopted. Note that the BEARS data are in the  $T_{\text{mb}}$  scale.

2. For the other data (in  $T_A^*$ ), the intensities corrected for the daily variation were obtained by multiplying the intensity data of the corresponding sub-box by the scaling factor of the daily variation  $SF_{\text{ref}}$ , where the scaling factor  $SF_{\text{ref}}$  is the ratio of the sum of the integrated intensity of the reference area obtained at the the corresponding observation session ( $S_{\text{ref}} = \sum_i I_{i,\text{ref}}$ ) to that obtained at the reference date ( $S_{\text{ref}}^* = \sum_i I_{i,\text{ref}}^*$ ,  $SF_{\text{ref}} = S_{\text{ref}}^*/S_{\text{ref}}$ ). Note that we observed a small reference area at least once during each observation session.
3. Then, the intensities corrected for daily variation were divided by the beam efficiency at the corresponding frequency and converted to intensities in the  $T_{\text{mb}}$  scale.

We describe the details of the procedure below.

## 4.1 Orion A

### 4.1.1 $^{12}\text{CO}$ and $^{13}\text{CO}$

The  $^{12}\text{CO}$  and  $^{13}\text{CO}$  maps obtained with BEARS cover the northern part of the FOREST observation areas shown in figure 1. The intensity scales of the  $^{12}\text{CO}$  and  $^{13}\text{CO}$  data were thus calibrated by comparing with the previous survey data taken by the BEARS receiver (Shimajiri et al. 2011, 2014; Nakamura et al. 2012), which were already corrected into the main beam temperature ( $T_{\text{mb}}$ ) scale. We obtained the intensities by dividing the FOREST intensities obtained in  $T_A^*$  by the scaling factor  $SF_i$  determined in each sub-box and each line using the equation

$$SF_i^{\text{BEARS},l} = \frac{\sum_{k=1}^{N_i} W_{k,\text{BEARS},l} / W_{k,\text{FOREST},l}}{N_i}, \quad (1)$$

where  $W_{k,\text{FOREST},l}$  is the integrated intensity of a given box in the antenna temperature scale at the  $k$ th grid, and  $W_{k,\text{BEARS},l}$  is the integrated intensity of the same box in the brightness temperature scale at the  $k$ th grid;  $l$  is the corresponding line, and  $N_i$  is the number of grids in the  $i$ th box. We measured the intensity ratio at every grid point and took an average in each sub-box. For almost all the boxes, the dispersions of the scaling factors were within  $3\sigma$  of the mean value of each observation season. For the boxes where the SF values were larger than  $3\sigma$  of the mean value or the boxes where the emission was too weak to measure the SF value, we adopted the value of SF measured immediately before or after the corresponding observation. However, we note that such sub-boxes with large dispersions were rare. The scaling factors so derived are consistent with the results of the measurements of the telescope main beam efficiencies. For example, in the 2015–2016 season, the mean value of the scaling factor was measured to about 2.1, which corresponds to the main beam efficiency of 0.48 at 115 GHz. The

actual main beam efficiency of the telescope was measured to be about 0.45.

Finally, we combined the FOREST  $^{12}\text{CO}$  and  $^{13}\text{CO}$  data with the BEARS data to reduce the noise levels. The data combination enabled us to typically reduce the noise levels by a factor of 1.5–2, which was crucial for making the CARMA and NRO combined Orion images, so that the noise levels in the  $uv$  space were well matched.

### 4.1.2 $\text{C}^{18}\text{O}$ , CCS, and $\text{N}_2\text{H}^+$

Since the map coverage of the  $\text{C}^{18}\text{O}$  data obtained with BEARS was not too large and we did not have the corresponding  $\text{N}_2\text{H}^+$  and CCS data, we applied a different intensity calibration procedure. For the  $\text{C}^{18}\text{O}$  and  $\text{N}_2\text{H}^+$  data we derived the daily scaling factors or daily intensity variations by observing a small area containing FIR 4, which was observed at every observation session once or twice. To determine the daily scaling factors we observed a small area containing FIR 3/4/5 at the date when the wind speed at the telescope site was almost zero and  $T_{\text{sys}}$  was close to the lowest value, and we adopted the integrated intensity of the FIR 3/4/5 area at that date as a reference. Immediately after this measurement we also observed a small area of B213 in Taurus to compare the data with those obtained with the IRAM 30 m telescope (Tafalla & Hacar 2015) to check the intensity accuracy. To compare the intensities taken with different telescopes, we smoothed the Nobeyama data to match the map effective angular resolution. Details of the FIR 3/4/5 area are given in Nakamura et al. (2019). For  $\text{C}^{18}\text{O}$ , we also checked the absolute intensity by using the  $\text{C}^{18}\text{O}$  map obtained with BEARS toward the northern part of Orion A (Shimajiri et al. 2014, 2015) and we confirmed that our FOREST  $\text{C}^{18}\text{O}$  intensities agree with the BEARS data within an error of less than 10%. For  $\text{N}_2\text{H}^+$ , we checked the absolute intensity by using the  $\text{N}_2\text{H}^+$  ( $J = 1-0$ ) fit data obtained with the IRAM 30 m telescope toward B213 in Taurus (Tafalla & Hacar 2015). We confirmed that the intensity of  $\text{N}_2\text{H}^+$  ( $J = 1-0$ ) in B213 obtained with FOREST was only about 5% larger than that of the IRAM value, where we divided the intensity in the antenna temperature scale by the main beam efficiency at 94 GHz. Thus, we consider that the intensity scale of the  $\text{N}_2\text{H}^+$  data is reasonably accurate.

For CCS, we simply divided the intensities in  $T_A^*$  by the main beam efficiency. The CCS emission is extremely weak for all the targets.

## 4.2 Aquila Rift and M 17

The BEARS maps of the Aquila Rift were only toward the Serpens South region and the map coverages are very small compared to the FOREST mapping areas. Therefore, we

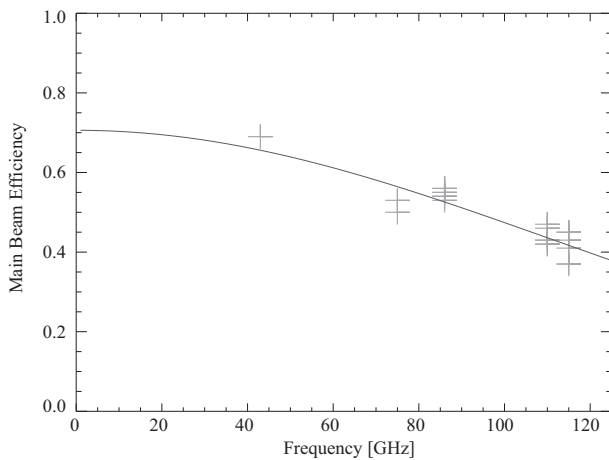


**Fig. 4.** Main beam efficiency of the Nobeyama 45 m telescope as a function of frequency. The crosses indicate the efficiencies measured with the receivers installed on the 45 m telescope. The red line shows the line fitted with equation (2).

did not combine the BEARS and FOREST data. Thus, we applied the same procedure as the Orion A C<sup>18</sup>O data calibration to make the <sup>12</sup>CO, <sup>13</sup>CO, C<sup>18</sup>O, and N<sub>2</sub>H<sup>+</sup> data of the Aquila Rift. After correcting the daily intensity variations of the FOREST data, we compared the FOREST intensities to the BEARS intensities toward Serpens South to determine the scaling factors. The scaling factors computed agreed with those determined with the main beam efficiencies within an error of ~5%–10%. For M17, we mapped small areas to measure the daily intensity variations and followed the same procedure as for the Aquila Rift.

### 4.3 Main beam efficiencies of the Nobeyama 45 m telescope

The Nobeyama Radio Observatory measures the main beam efficiencies of the telescope at several frequencies every season, except for the 2016–2017 season which was our last (third) season. Planets such as Mars or Jupiter are often used for the measurements—see the web page of the observatory for details of the measurements. Here, we obtain the main beam efficiencies of the observed lines by fitting the values measured with several receivers on the 45 m telescope.

In figure 4 we show the telescope main beam efficiency measured in the 2015–2016 season. We plotted all the values of the main beam efficiencies measured with the available receivers installed on the 45 m telescope. By fitting the data points with the function

$$\eta_A = \eta_{A0} \times \exp \left[ - \left( \frac{4\pi\epsilon}{\lambda} \right)^2 \right] \quad (2)$$

we derived the main beam efficiencies at the frequencies of our target molecular lines using a least-squares fit; we obtained  $\eta_{A0} = 0.539$ , and the accuracy of the parabola surface is given as  $\epsilon = 0.151$  mm. The derived main beam efficiencies are summarized in the last column of table 3. This procedure is basically the same as the one recommended by the observatory.

We used the obtained main beam efficiencies to convert the intensities measured in the antenna temperature scale into those in the brightness temperature scale, except for <sup>12</sup>CO and <sup>13</sup>CO of Orion A.

## 5 Global molecular gas distribution

In this section we present the global molecular gas distribution toward the three target clouds. The detailed characteristics, particularly the velocity structures, of the individual clouds will be described in separate papers.

### 5.1 Average spectra of the three clouds

In figure 5 we present the average spectra of the CO lines for the three clouds. For Orion A, the average spectrum of the <sup>12</sup>CO emission line has a single peak. There are three peaks or shoulders in <sup>13</sup>CO and C<sup>18</sup>O at around 7 km s<sup>-1</sup>, 9 km s<sup>-1</sup>, and 11 km s<sup>-1</sup>. The Orion A filament has a large velocity gradient toward the northern part, and these components are affected by the global velocity gradient along the filament. However, roughly speaking, the 11 km s<sup>-1</sup> component is dominant toward the northern part, while the 7 km s<sup>-1</sup> component appears in the southern part. The 9 km s<sup>-1</sup> component is strong in the main filamentary structure.

For the other two regions, the spectra have multiple peaks. For Aquila Rift and M17, <sup>12</sup>CO has at least three major peaks. For Aquila Rift, the C<sup>18</sup>O has a single peak at 7.3 km s<sup>-1</sup> and thus the dips seen in <sup>12</sup>CO and <sup>13</sup>CO are expected to be due to self-absorption (Shimoikura et al. 2018). The weak but distinct component at around 40 km s<sup>-1</sup> may be the molecular gas influenced by a superbubble created by star formation in the Scorpius–Centaurus Association (Breitschwerdt et al. 1996; Frisch et al. 2015). This component is seen in <sup>13</sup>CO but it is difficult to recognize in C<sup>18</sup>O. The <sup>12</sup>CO profile has a tail between 10 km s<sup>-1</sup> and 35 km s<sup>-1</sup>. This comes from several different components which reside in this region. These components are more prominent in the average spectra of smaller areas and we will discuss them later in a separate paper. These complicated molecular gas distributions may be due to the interaction of molecular clouds with superbubbles (Frisch 1998; Frisch et al. 2015; Nakamura et al. 2017).

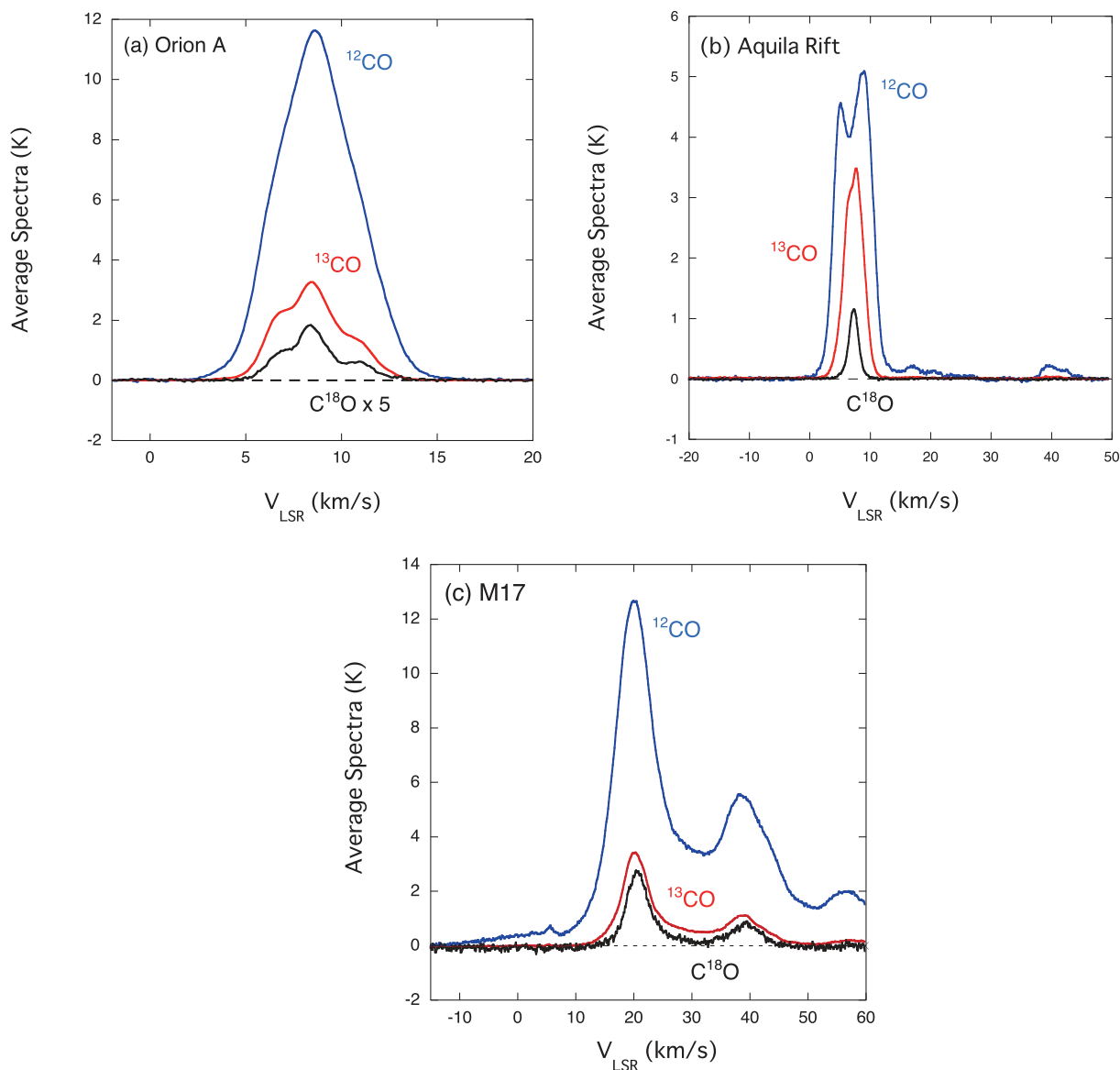


**Fig. 5.** Average spectra of  $^{12}\text{CO}$ ,  $^{13}\text{CO}$ , and  $\text{C}^{18}\text{O}$  toward (a) Orion A, (b) Aquila Rift, and (c) M17. The blue, red, and black lines indicate the  $^{12}\text{CO}$ ,  $^{13}\text{CO}$ , and  $\text{C}^{18}\text{O}$  spectra, respectively. (Color online)

For M17, the three components of  $\sim 20 \text{ km s}^{-1}$ ,  $\sim 40 \text{ km s}^{-1}$ , and  $\sim 55 \text{ km s}^{-1}$  are the molecular gas components which belong to the Sagittarius, Scutum, and Norma arms, respectively (Zucker et al. 2015), as discussed by Nguyen Luong et al. (2019), and the main component is the one at  $20 \text{ km s}^{-1}$  where NGC 6811 and M17 SWex are located.

## 5.2 Orion A

Figures 6, 7, 8, 9, and 10 show the integrated intensity maps of Orion A for  $^{12}\text{CO}$  ( $J = 1-0$ ),  $^{13}\text{CO}$  ( $J = 1-0$ ),  $\text{C}^{18}\text{O}$  ( $J = 1-0$ ),  $\text{N}_2\text{H}^+$  ( $J = 1-0$ ), and  $\text{CCS}$  ( $J = 8_7-7_6$ ), respectively. For comparison, we have overlaid the contours of the Herschel  $\text{H}_2$  column density map on the

integrated intensity image in the right panel of each figure. Each map except  $\text{N}_2\text{H}^+$  is integrated from  $2 \text{ km s}^{-1}$  to  $20 \text{ km s}^{-1}$ . For  $\text{N}_2\text{H}^+$ , we integrated the emission from  $0 \text{ km s}^{-1}$  to  $22 \text{ km s}^{-1}$  so that all seven hyperfine components are summed. Our maps cover a region from OMC-3 to NGC 1999, spanning about  $2^\circ$  in declination. The results of our protostellar outflow survey and cloud structure analysis are given in separate papers (Tanabe et al. 2019; Ishii et al. 2019; H. Takemura et al. in preparation).

Figures 6, 7, and 8 show that the  $^{12}\text{CO}$ ,  $^{13}\text{CO}$ , and  $\text{C}^{18}\text{O}$  emissions trace the areas with column density higher than  $\sim 0.5 \times 10^{22} \text{ cm}^{-2}$ ,  $\sim 0.75 \times 10^{22} \text{ cm}^{-2}$ , and  $\sim 2.5 \times 10^{22} \text{ cm}^{-2}$ , respectively.  $\text{N}_2\text{H}^+$  emission comes from the area with column density larger than  $\sim 5 \times 10^{22} \text{ cm}^{-2}$  (see figure 9).

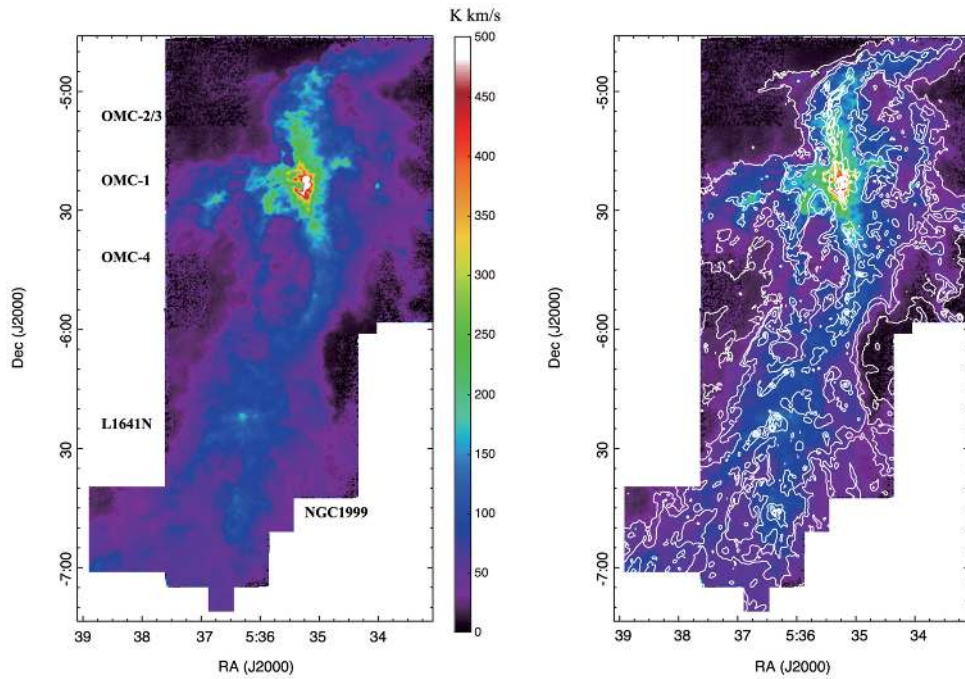


**Fig. 6.** (a)  $^{12}\text{CO}$  ( $J = 1-0$ ) moment-0 map of Orion A, velocity-integrated from  $2 \text{ km s}^{-1}$  to  $20 \text{ km s}^{-1}$ . (b) Same as panel (a), but the contours of the  $\text{H}_2$  column density are overlaid on the image. The contour levels are  $2.5 \times 10^{21} \text{ cm}^{-2}$ ,  $5.0 \times 10^{21} \text{ cm}^{-2}$ ,  $7.5 \times 10^{21} \text{ cm}^{-2}$ ,  $2.5 \times 10^{22} \text{ cm}^{-2}$ ,  $5.0 \times 10^{22} \text{ cm}^{-2}$ ,  $7.5 \times 10^{22} \text{ cm}^{-2}$ , ... The effective angular resolution of the  $^{12}\text{CO}$  map is  $21''.7$ . (Color online)

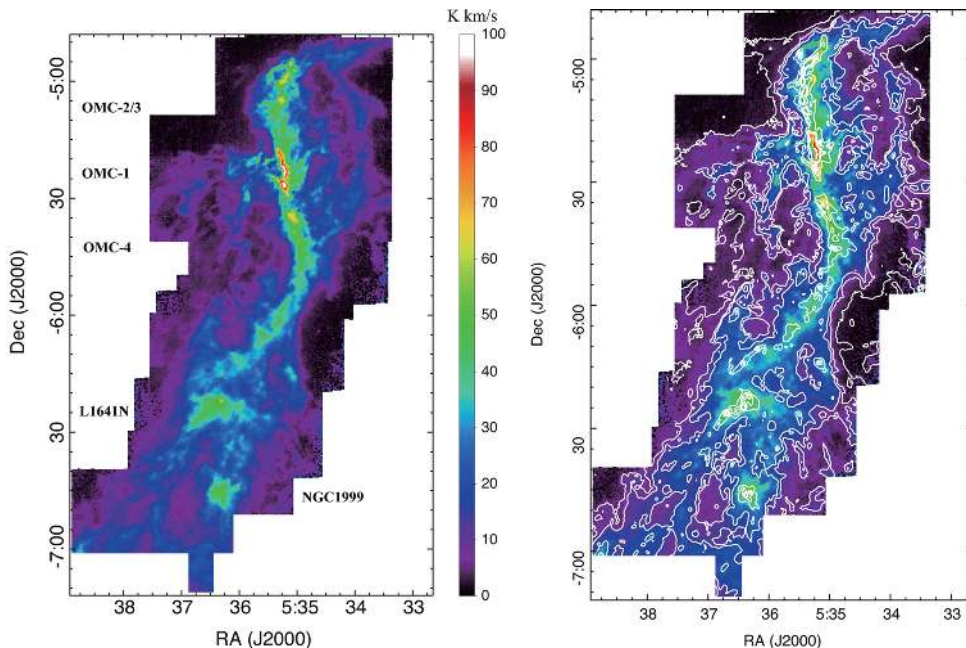


**Fig. 7.** (a)  $^{13}\text{CO}$  ( $J = 1-0$ ) moment-0 map of Orion A, velocity-integrated from  $2 \text{ km s}^{-1}$  to  $20 \text{ km s}^{-1}$ . (b) Same as panel (a) but the contours of the  $\text{H}_2$  column density are overlaid on the image. The contour levels are the same as those of figure 6. The effective angular resolution of the  $^{13}\text{CO}$  map is  $22''.1$ . (Color online)

In figure 10 we show the integrated intensity map of CCS, where the image was smoothed with an effective angular resolution of  $32''$  to improve the signal-to-noise ratio. The CCS emission is detected significantly only in

the OMC-1 region where the strong  $\text{C}^{18}\text{O}$  and  $\text{N}_2\text{H}^+$  emission is detected. Our CCS map is the first unbiased CCS map of Orion A with the  $J_N = 8_7-7_6$  line. Previous wide-field maps were taken only toward the main filament with

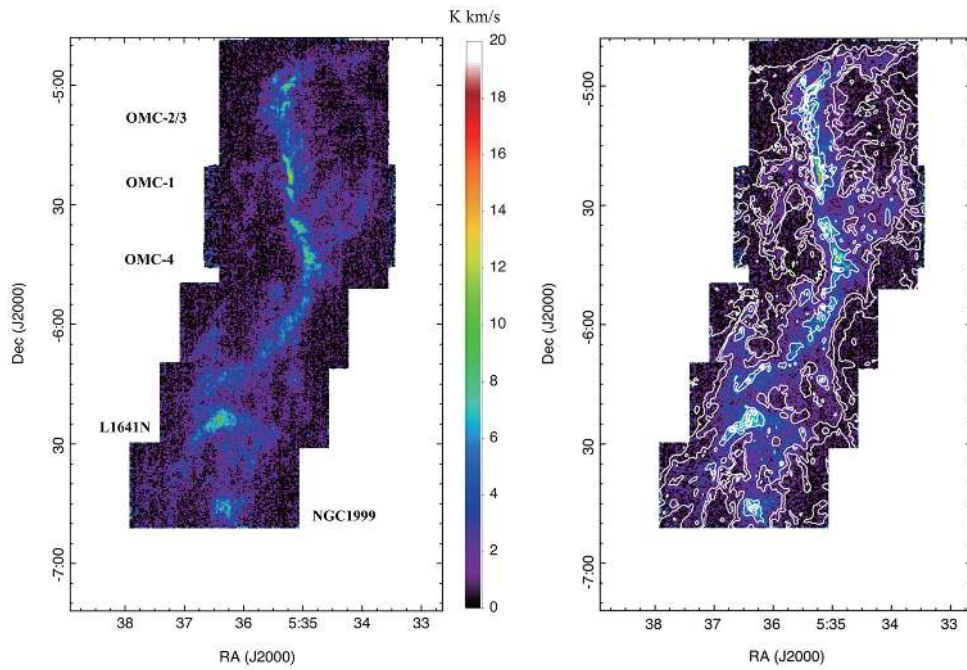


**Fig. 8.** (a)  $\text{C}^{18}\text{O}$  ( $J = 1-0$ ) moment-0 map of Orion A, velocity-integrated from  $2 \text{ km s}^{-1}$  to  $20 \text{ km s}^{-1}$ . (b) Same as panel (a), but the contours of the  $\text{H}_2$  column density are overlaid on the image. The contour levels are the same as those of figure 6. The effective angular resolution of the  $\text{C}^{18}\text{O}$  map is  $22''.1$ . (Color online)

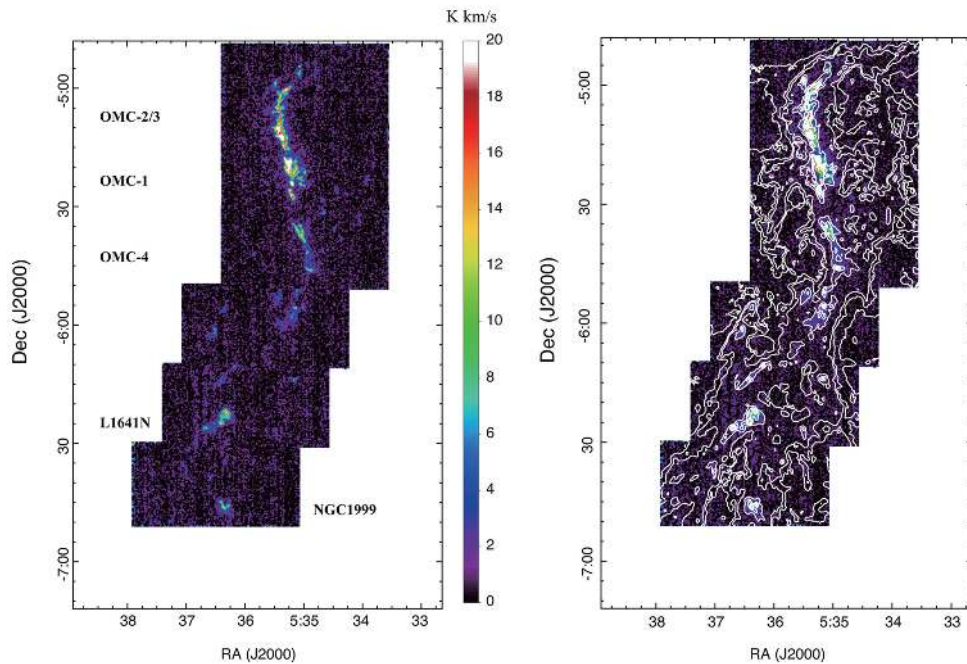


**Fig. 9.** (a)  $\text{N}_2\text{H}^+$  ( $J = 1-0$ ) velocity integrated map of Orion A. The integration range is from  $0 \text{ km s}^{-1}$  to  $20 \text{ km s}^{-1}$ . (b) Same as panel (a), but the contours of the  $\text{H}_2$  column density are overlaid on the image. The contour levels are the same as those of figure 6. The effective angular resolution of the  $\text{N}_2\text{H}^+$  map is  $24''.1$ . (Color online)

other transition lines ( $J_N = 4_3-3_2$  at 45 GHz and  $J_N = 7_6-6_5$  at 81.5 GHz) by Tatematsu et al. (2008, 2014). CCS is known to trace dense gas with densities of  $10^4 \text{ cm}^{-3}$ , but the abundance of CCS decreases very rapidly due to the destruction. In Orion A, the CCS emission is very weak. Only

toward the OMC-1 region we detect the emission with a signal-to-noise ratio of  $5\sigma$ . Weaker emission is sometimes seen along the ridge. This weak CCS emission implies that Orion A is a relatively evolved molecular cloud. We note that CCS is detected in the OMC-2 FIR 4 region for much

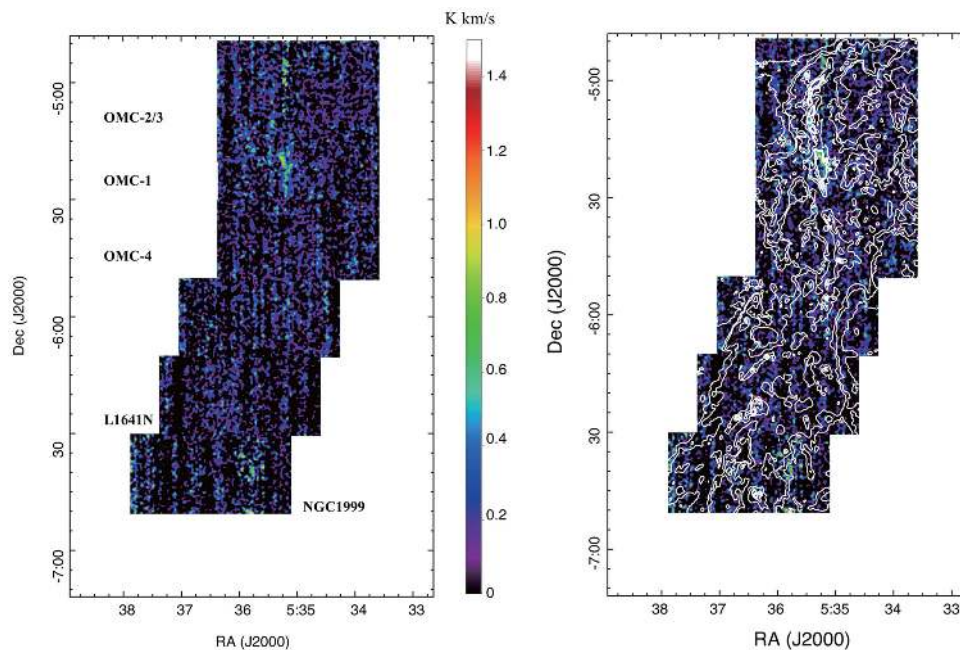


**Fig. 10.** CCS integrated intensity map of Orion A. We smoothed the CCS image with an effective angular resolution of  $32''$ . The contour levels are the same as those of figure 6. The effective angular resolution of the CCS map is  $24''$ . (Color online)

higher-sensitivity observations (Nakamura et al. 2019). The OMC-1 region may be relatively chemically young compared to other parts in Orion A. Recently, Hacar et al. (2017) proposed that the OMC-1 region is gravitationally contracting along the main filament. Such a global infall motion can be recognized in our  $^{13}\text{CO}$  data (Ishii et al. 2019). If OMC-1 is indeed infalling toward the center, the gas is continuously fed along the main filament in OMC-1. Thus, the significant CCS emission in OMC-1 may come from the material newly fed from outside by the gravitational contraction.

Figure 9 shows the  $\text{N}_2\text{H}^+$  map of the Orion A molecular cloud. The map is consistent with the image taken by Tatematsu et al. (2008), who mapped the Orion A filament in a position-switch mode with full-beam sampling, using the BEARS receiver. Our mapping area is much wider than theirs. Also, since we mapped Orion A in the OTF mode, the angular resolution is somewhat better than that of Tatematsu et al. (2008). The  $\text{N}_2\text{H}^+$  emission is stronger in the northern part (OMC-1, OMC-2, and OMC-3) and traces the main filamentary structure running in the north-south direction. Our  $\text{N}_2\text{H}^+$  map shows that many faint  $\text{N}_2\text{H}^+$  cores are distributed outside the main filament as well.

### 5.3 Aquila Rift

Figures 11, 12, 13, 14, and 15 show the integrated intensity maps of the Aquila Rift for  $^{12}\text{CO}$  ( $J = 1-0$ ),  $^{13}\text{CO}$  ( $J = 1-0$ ),  $\text{C}^{18}\text{O}$  ( $J = 1-0$ ),  $\text{N}_2\text{H}^+$  ( $J = 1-0$ ), and CCS

( $J = 7_6-6_5$ ), respectively. Each map except  $\text{N}_2\text{H}^+$  is integrated from  $-10 \text{ km s}^{-1}$  to  $45 \text{ km s}^{-1}$ . For  $\text{N}_2\text{H}^+$ , we integrated all seven hyperfine components to produce the intensity map.

The  $^{12}\text{CO}$  emission is strongest toward the W 40 region and the Serpens South cluster. The  $^{13}\text{CO}$  emission traces an arc-like structure in the W 40 region. However, the filamentary structures, particularly toward the Serpens South region, are difficult to recognize in the  $^{12}\text{CO}$  and  $^{13}\text{CO}$  images. From the  $\text{C}^{18}\text{O}$  image, we can vaguely find the filamentary structures in Serpens South. The filamentary structures detected by the Herschel map are prominent toward Serpens South in  $\text{N}_2\text{H}^+$

A prominent linear structure is seen in the northeast part of the observed area from W 40 in the  $^{13}\text{CO}$  map. This  $^{13}\text{CO}$  structure is less prominent in the Herschel column density map. This structure may be created by the interaction of the molecular cloud and the W 40 H II region. Similar linear structures are seen in  $\text{C}^{18}\text{O}$  at different parts of the mapped area. In figure 16, we compare the  $250 \mu\text{m}$  Herschel image (gray scale) with the  $^{13}\text{CO}$  image velocity-integrated from  $5.0 \text{ km s}^{-1}$  to  $6.6 \text{ km s}^{-1}$  (contours). Weak  $250 \mu\text{m}$  emission appears to trace the  $^{13}\text{CO}$  linear structure. See Shimoikura et al. (2019b) for details of the cloud structure and properties of the Aquila Rift. The  $^{12}\text{CO}$  integrated intensity map indicates the presence of protostellar outflows, particularly in the Serpens South protocluster region (see also Nakamura et al. 2011a; Shimoikura et al. 2015). In section 7 we present the results of the outflow survey toward the Serpens South region. The CCS emission is weak, but

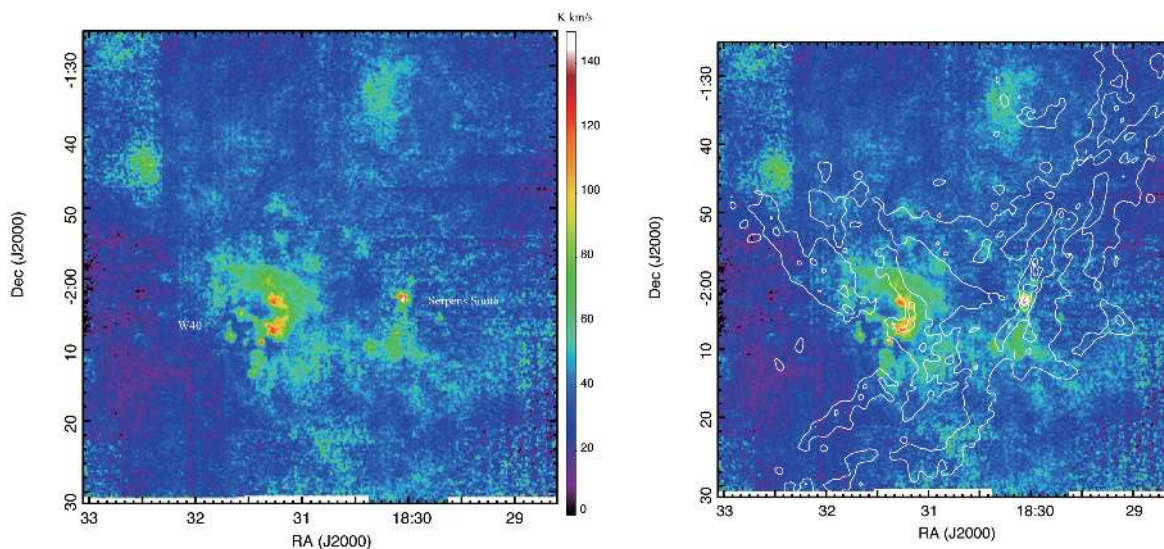


**Fig. 11.**  $^{12}\text{CO}$  ( $J = 1-0$ ) integrated intensity map of the Aquila Rift. In the panel (b), the contour levels are  $1.0 \times 10^{22} \text{ cm}^{-2}$ ,  $2.5 \times 10^{22} \text{ cm}^{-2}$ ,  $5.0 \times 10^{22} \text{ cm}^{-2}$ ,  $7.5 \times 10^{22} \text{ cm}^{-2}$ ,  $1.0 \times 10^{23} \text{ cm}^{-2}$ ,  $1.5 \times 10^{23} \text{ cm}^{-2}$ . The effective angular resolution of the  $^{12}\text{CO}$  map is  $21''.7$ . (Color online)

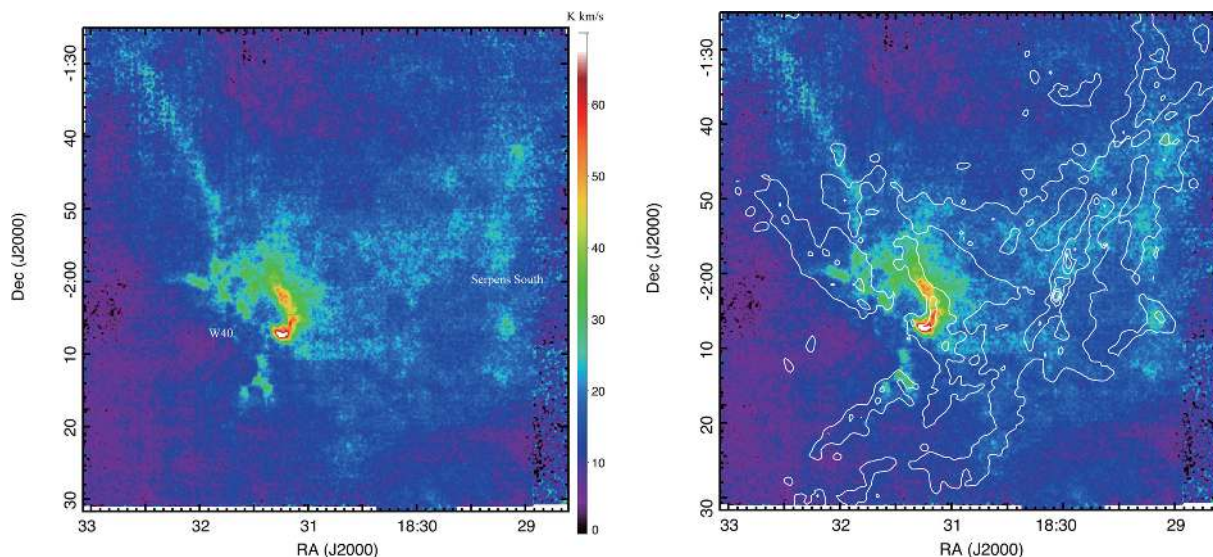


**Fig. 12.**  $^{13}\text{CO}$  ( $J = 1-0$ ) integrated intensity map of the Aquila Rift. The contour levels are the same as those of figure 11. The effective angular resolution of the  $^{13}\text{CO}$  map is  $22''.1$ . (Color online)

significant emission comes along the Serpens South filament. This indicates that the Serpens South filaments are chemically relatively young.

### 5.3.1 M17

Figures 17, 18, 19, and 20 show the integrated intensity maps of M17 for  $^{12}\text{CO}$  ( $J = 1-0$ ),  $^{13}\text{CO}$  ( $J = 1-0$ ),  $\text{C}^{18}\text{O}$  ( $J = 1-0$ ), and  $\text{N}_2\text{H}^+$  ( $J = 1-0$ ), respectively. Each map except  $\text{N}_2\text{H}^+$  is integrated from  $-10$  to  $60 \text{ km s}^{-1}$ . We could not detect significant CCS emission, and thus we do not show the CCS integrated intensity map. For  $\text{N}_2\text{H}^+$  we integrated all seven hyperfine components to make an integrated intensity map.

The  $^{12}\text{CO}$  and  $^{13}\text{CO}$  emission is strongest toward the M17 H II region. The emission lines are spatially extended toward the M17 SWex region, whose dense parts are detected in  $\text{C}^{18}\text{O}$ . The  $\text{N}_2\text{H}^+$  emission is spatially localized and seen as blobs. The detailed cloud structure and kinematics will be discussed in separate papers (e.g., Shimoikura et al. 2019a).

## 6 Spatial variation of the fractional abundances of $^{13}\text{CO}$ and $\text{C}^{18}\text{O}$

Here, using  $^{12}\text{CO}$ ,  $^{13}\text{CO}$ , and  $\text{C}^{18}\text{O}$ , we derive physical quantities such as the excitation temperature, fractional



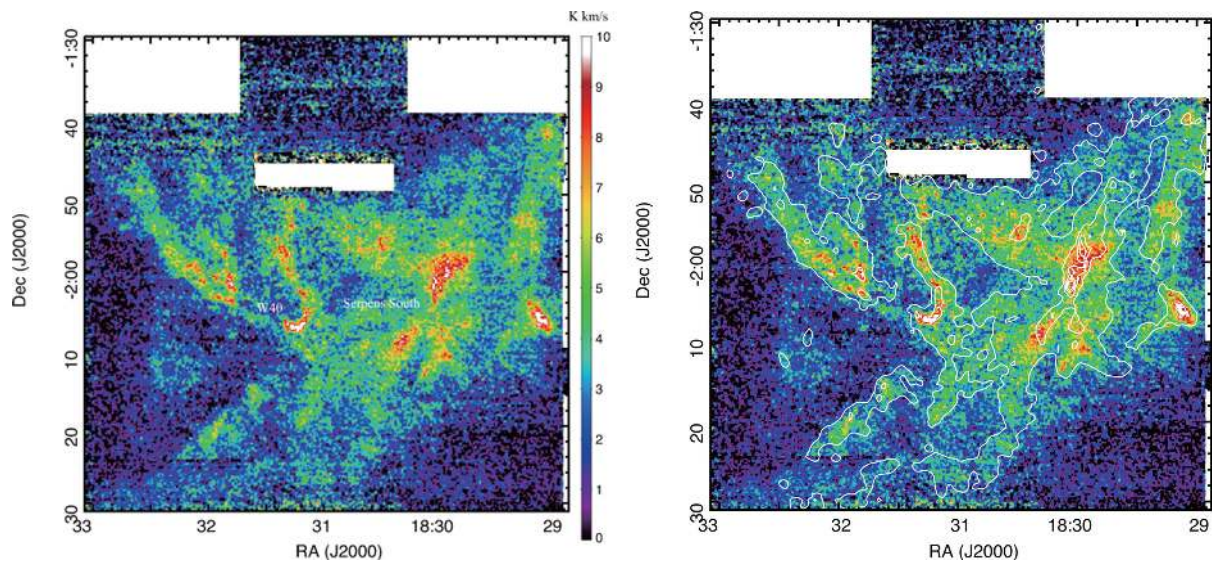


**Fig. 13.**  $\text{C}^{18}\text{O}$  ( $J = 1-0$ ) integrated intensity map of the Aquila Rift. The contour levels are the same as those of figure 11. The effective angular resolution of the  $\text{C}^{18}\text{O}$  map is  $22''.1$ . (Color online)

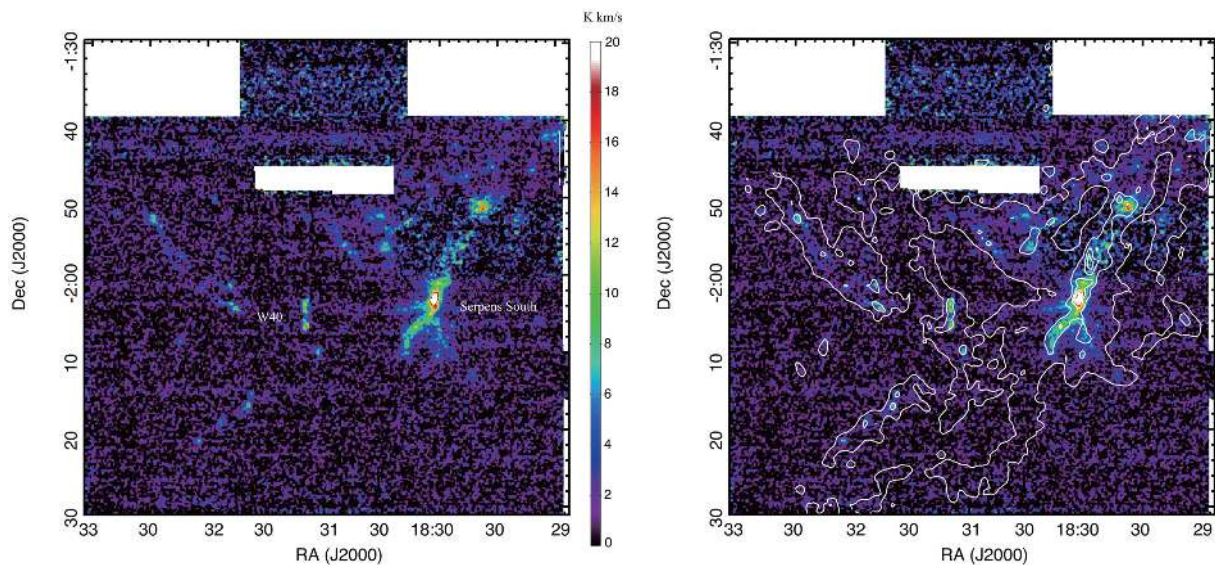


**Fig. 14.**  $\text{N}_2\text{H}^+$  ( $J = 1-0$ ) integrated intensity map of the Aquila Rift. The contour levels are the same as those of figure 11. The effective angular resolution of the  $\text{N}_2\text{H}^+$  map is  $24''.1$ . (Color online)

abundances, and optical depth toward Orion A. The detailed analysis is presented in Ishii et al. (2019). See separate papers for the results of the other regions.

### 6.1 Derivation of excitation temperature, optical depth, and column density of CO

Here, we derive excitation temperature, optical depth, and  $^{13}\text{CO}$  and  $\text{C}^{18}\text{O}$  column densities toward Orion A. First, we describe how we derive the physical quantities from our data, and then briefly present the spatial distributions of the physical quantities for Orion A.

Assuming that the  $^{12}\text{CO}$  ( $J = 1-0$ ) line is optically thick, we derive the excitation temperature  $T_{\text{ex}}$  using the following equation (see, e.g., Pineda et al. 2008; Shimajiri et al. 2011; Ishii et al. 2019):

$$T_{\text{ex}} = \frac{5.53}{\ln[1 + 5.53/(T_{\text{peak}} + 0.819)]} \text{K}, \quad (3)$$

where  $T_{\text{peak}}$  is the maximum intensity along the line of sight. We also assumed that the excitation temperatures of  $^{13}\text{CO}$  and  $\text{C}^{18}\text{O}$  are the same as  $T_{\text{ex}}$  calculated with the above equation. We note that the excitation temperature of  $^{12}\text{CO}$ ,

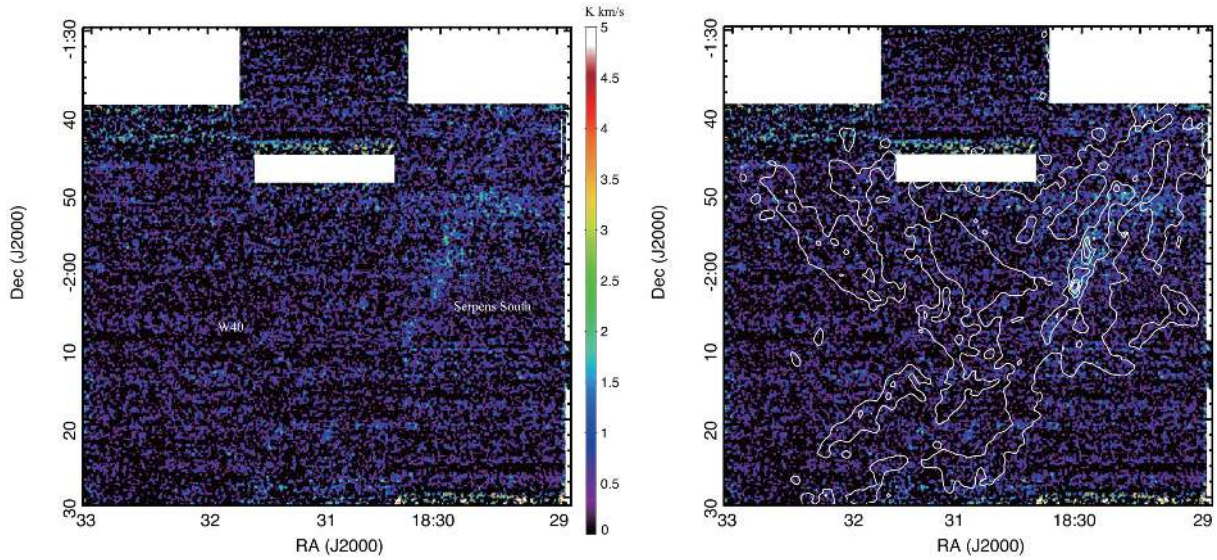


**Fig. 15.** CCS ( $J = 87-76$ ) integrated intensity map of the Aquila Rift. The contour levels are the same as those of figure 11. The effective angular resolution of the CCS map is  $24''.0$ . (Color online)

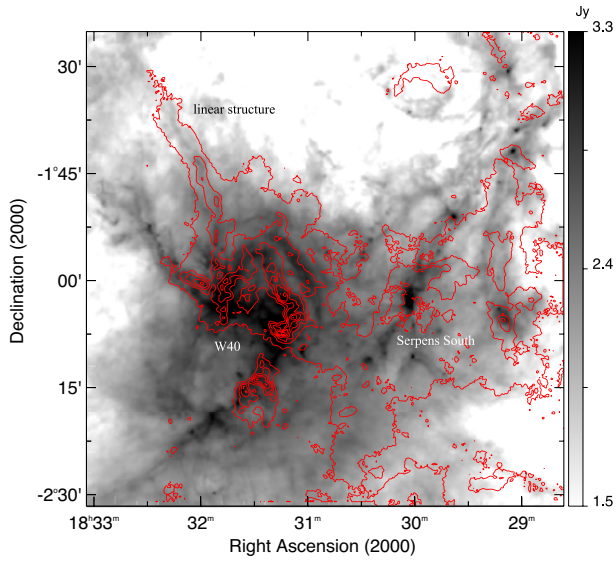


**Fig. 16.** The  $^{13}\text{CO}$  intensity map overlaid on the Herschel  $250\ \mu\text{m}$  image. The integration range of the  $^{13}\text{CO}$  is from  $5.0\ \text{km s}^{-1}$  to  $6.6\ \text{km s}^{-1}$ . The contours start at  $4.0\ \text{K km s}^{-1}$  with an interval of  $4.0\ \text{K km s}^{-1}$ . (Color online)

which is likely to be close to LTE, can be used as a good measure of the gas temperature.

The optical depths and column densities for each channel are derived with the following formulas:

$$\tau_{^{13}\text{CO}} = -\ln \left\{ 1 - \frac{T_{^{13}\text{CO}}}{5.29[J(T_{\text{ex}}) - 0.164]} \right\}, \quad (4)$$

$$N_{^{13}\text{CO}} = 2.42 \times 10^{14} \left[ \frac{\tau_{^{13}\text{CO}} T_{\text{ex}} \Delta V}{1 - \exp(-5.29/T_{\text{ex}})} \right] \text{cm}^{-2}, \quad (5)$$

$$\tau_{\text{C}^{18}\text{O}} = -\ln \left\{ 1 - \frac{T_{\text{C}^{18}\text{O}}}{5.27[J(T_{\text{ex}}) - 0.164]} \right\}, \quad (6)$$

and

$$N_{\text{C}^{18}\text{O}} = 2.42 \times 10^{14} \left[ \frac{\tau_{\text{C}^{18}\text{O}} T_{\text{ex}} \Delta V}{1 - \exp(-5.27/T_{\text{ex}})} \right] \text{cm}^{-2}, \quad (7)$$

where we assumed that the rotational transition is in the LTE. Here,  $\Delta V$  is the velocity resolution. The beam filling factors of  $^{13}\text{CO}$  and  $\text{C}^{18}\text{O}$  are set to unity. The function  $J_X(T)$  is given by  $[\exp(5.29/T) - 1]^{-1}$  and  $[\exp(5.27/T) - 1]^{-1}$  for  $^{13}\text{CO}$  and  $\text{C}^{18}\text{O}$ , respectively. To derive the opacity-corrected total column densities (Pineda et al. 2008), we summed the column density at each channel along the line of sight and multiplied the column densities by the correction factor of  $\tau_i/[1 - \exp(-\tau_i)]$ , where  $i$  is either  $^{13}\text{CO}$  or  $\text{C}^{18}\text{O}$ . The opacity-corrected total  $\text{H}_2$  column density is then derived from the  $^{13}\text{CO}$  integrated intensity assuming a constant abundance of  $2 \times 10^{-6}$  (Dickman 1978). We also derived the  $^{13}\text{CO}$  and  $\text{C}^{18}\text{O}$  fractional abundances relative to  $\text{H}_2$  by dividing the column densities by the Herschel  $\text{H}_2$  column density. See also Ishii et al. (2019) for these derivations for Orion A.

We summarize the molecular gas mass derived from  $^{13}\text{CO}$  in table 9. The total masses of the observed areas are estimated to be  $2.67 \times 10^4 M_\odot$ ,  $3.86 \times 10^4 M_\odot$ , and  $8.1 \times 10^5 M_\odot$  for Orion A, Aquila Rift, and M 17, respectively.

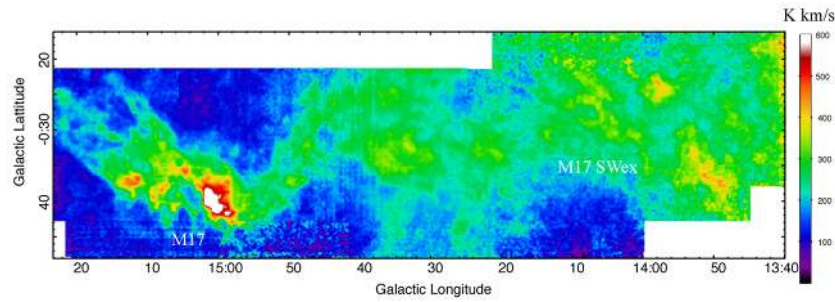


Fig. 17.  $^{12}\text{CO}$  ( $J = 1-0$ ) integrated intensity map of M17. The effective angular resolution of the  $^{12}\text{CO}$  map is  $21''.7$ . (Color online)

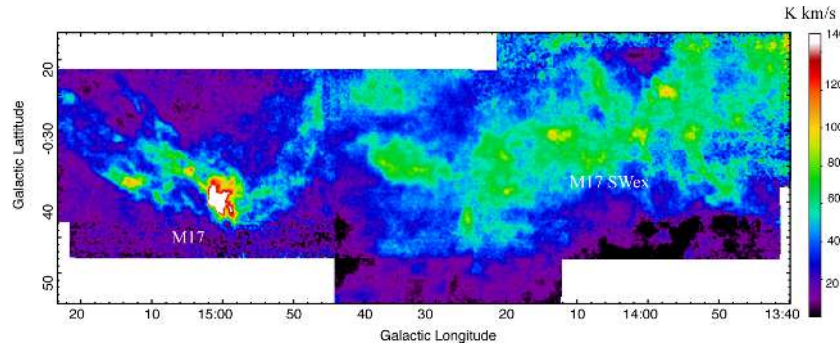


Fig. 18.  $^{13}\text{CO}$  ( $J = 1-0$ ) integrated intensity map of M17. The effective angular resolution of the  $^{13}\text{CO}$  map is  $22''.1$ . (Color online)

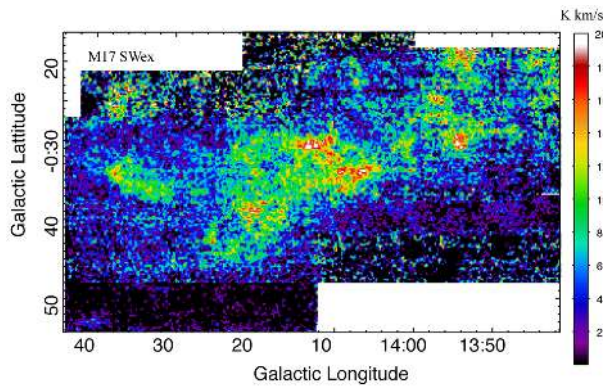


Fig. 19.  $\text{C}^{18}\text{O}$  ( $J = 1-0$ ) integrated intensity map of M17. The effective angular resolution of the  $\text{C}^{18}\text{O}$  map is  $22''.1$ . (Color online)

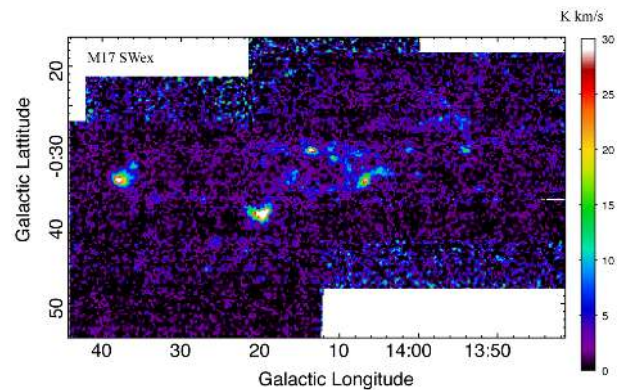


Fig. 20.  $\text{N}_2\text{H}^+$  ( $J = 1-0$ ) integrated intensity map of M17. The effective angular resolution of the  $\text{N}_2\text{H}^+$  map is  $24''.1$ . (Color online)

### 6.1.1 Orion A

In figure 21 we present the excitation temperature map of Orion A determined by the  $^{12}\text{CO}$  peak intensity. The excitation temperature ranges from  $\sim 8\text{ K}$  to  $\sim 100\text{ K}$ , and takes its maximum near Orion KL. The main filament has somewhat higher temperatures at  $\sim 50\text{ K}$  in the northern region. The southern part including L 1641 N and NGC 1999 has somewhat lower temperature at  $10\text{--}20\text{ K}$ . This temperature distribution is consistent with that of Kong et al. (2018) with a finer angular resolution.

The excitation temperature derived from  $^{12}\text{CO}$  tends to be somewhat higher than the dust temperature derived from the spectral energy distribution (SED) of the Herschel data.

In figure 22 we show the ratio of the excitation temperature derived from  $^{12}\text{CO}$  to the dust temperature. Here, we smoothed the excitation temperature map with an effective angular resolution of  $36''$  to match the effective resolution of the dust temperature map. The ratio stays at around two along the main filament, except in OMC-1 where the ratio is about five.

Figures 23, 24, and 25 show the spatial distributions of the opacity-corrected  $^{13}\text{CO}$  column density, the fractional abundances relative to  $\text{H}_2$ , and the optical depth for  $^{13}\text{CO}$  ( $J = 1-0$ ) and  $\text{C}^{18}\text{O}$  ( $J = 1-0$ ), respectively. The optical depth of  $^{13}\text{CO}$  ranges from a few to unity. It is about unity along

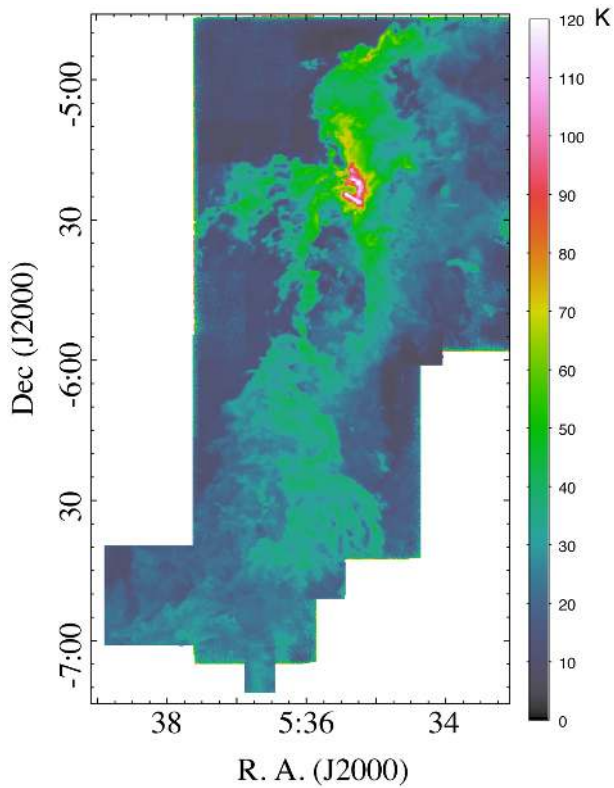


Fig. 21. Excitation temperature map of Orion A. (Color online)

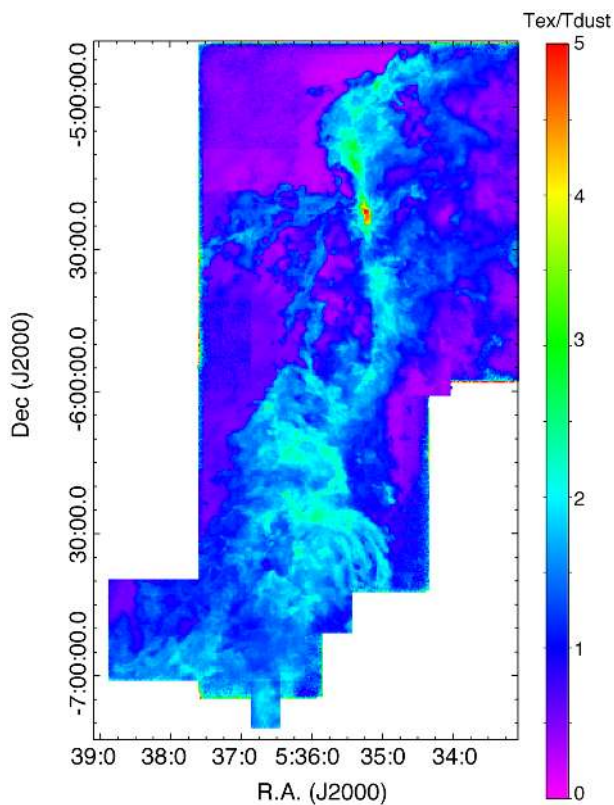


Fig. 22. Ratio of the excitation temperature derived from  $^{12}\text{CO}$  to the dust temperature derived from the Herschel data. The ratio is around 1–2 along the main ridge of Orion A, except in OMC-1. (Color online)

Table 9. Molecular gas mass estimated from  $^{13}\text{CO}$  toward Orion A, Aquila Rift, and M 17.\*

Name	Region	Mass ( $M_{\odot}$ )
Orion A	total	$3.86 \times 10^4$
Orion A North	$\text{Dec} \geq -05:30:26.0$	$1.56 \times 10^4$
Orion A South	$\text{Dec} \leq -05:16:03.5$	$2.30 \times 10^4$
Orion A OMC-1	$-05:30:26.0 \leq \text{Dec} \leq -0.5:16:03.5$	$7.4 \times 10^3$
Aquila Rift	total	$2.67 \times 10^4$
Aquila East (W 40)	$\text{RA} \leq 18:30:39.6$	$1.30 \times 10^4$
Aquila West (Serpens South)	$\text{RA} \geq 18:30:39.6$	$1.37 \times 10^4$
M 17	total	$8.1 \times 10^5$
M 17	$l \geq 14:26:22.5$	$3.6 \times 10^5$
M 17 SWex	$l \leq 14:26:22.5$	$4.5 \times 10^5$

\*OMC-1 is part of the north area of Orion A. The distances of 414 pc, 436 pc, and 2.0 kpc are adopted for Orion A, Aquila Rift, and M 17, respectively. The excitation temperature of  $^{13}\text{CO}$  is estimated from the peak intensity of  $^{12}\text{CO}$  at each pixel.

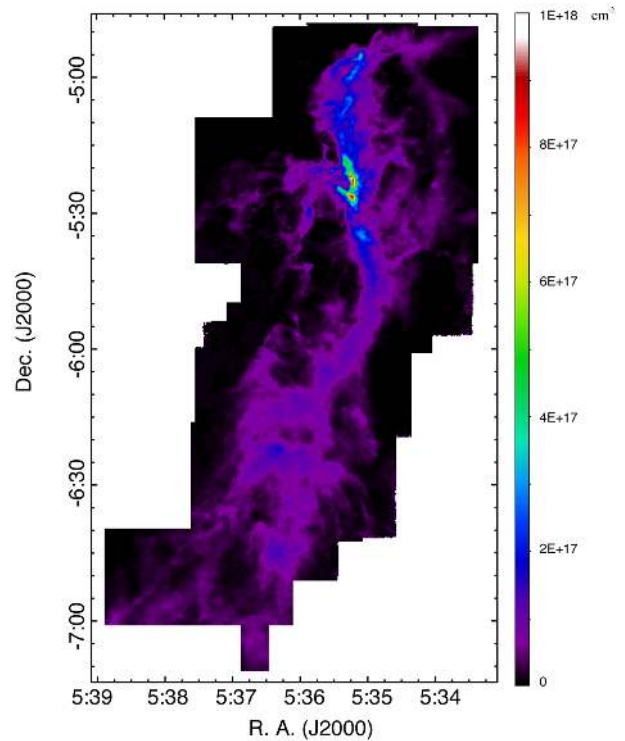


Fig. 23. Opacity-corrected  $^{13}\text{CO}$  column density map of Orion A. (Color online)

the filament. Several compact regions such as L 1641 N have larger optical depth at  $\sim 3$ . On the other hand, the optical depth of  $\text{C}^{18}\text{O}$  is less than unity for almost all areas. Thus, the  $\text{C}^{18}\text{O}$  emission is reasonably optically thin for the entire cloud.

The fractional abundance of  $^{13}\text{CO}$  ranges from a few  $\times 10^{-7}$  to a few  $\times 10^{-6}$ . It tends to be small, being  $5 \times 10^{-7}$  toward some dense areas such as the main filament

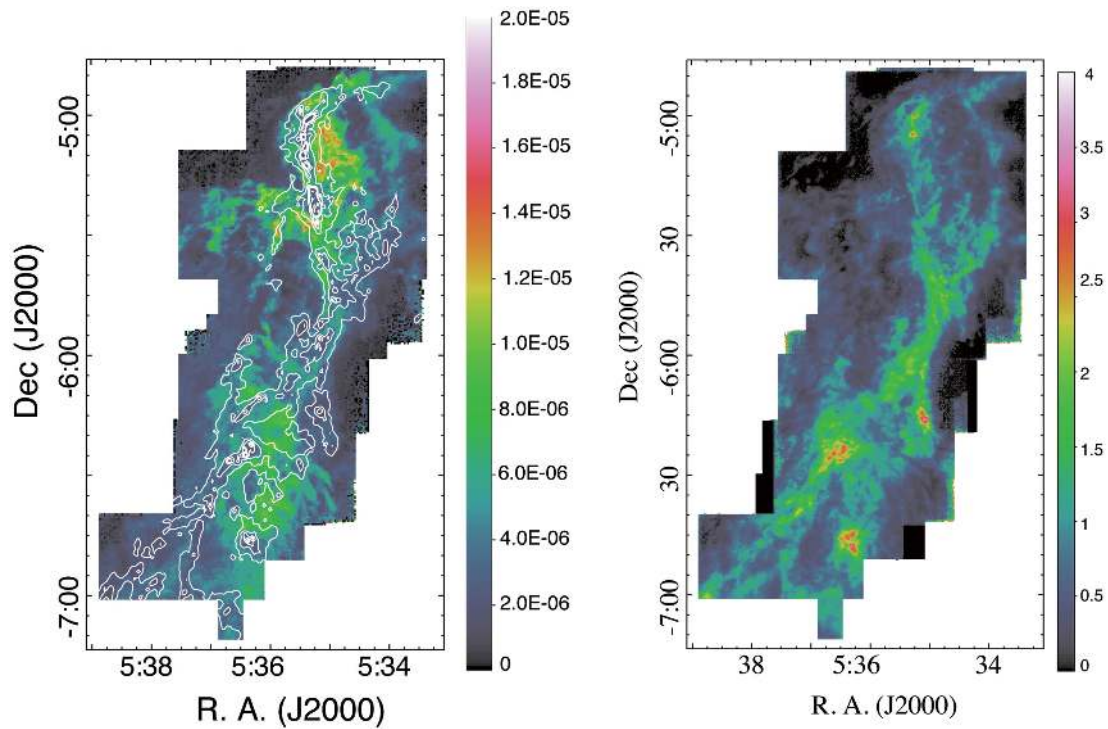


Fig. 24. (a)  $^{13}\text{CO}$  fractional abundance and (b) its optical depth maps of Orion A. (Color online)

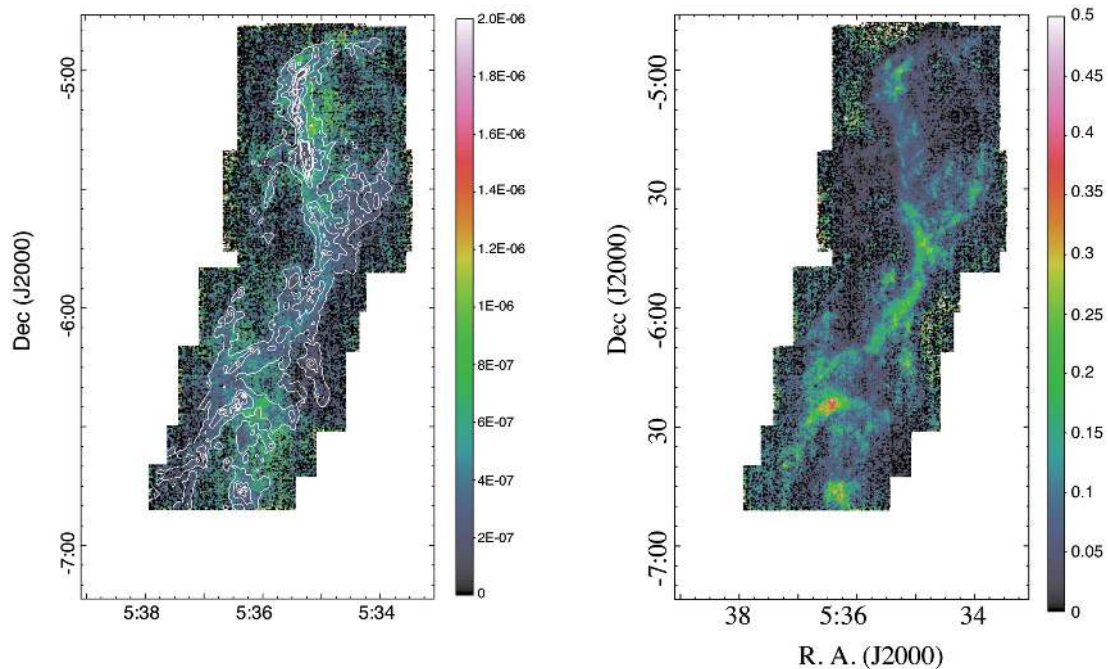


Fig. 25. (a)  $\text{C}^{18}\text{O}$  fractional abundance and (b) its optical depth maps of Orion A. (Color online)

of OMC-1/2/3 and L 1641 N. Outside the dense areas, the abundance goes up to a few  $\times 10^{-6}$ . For  $\text{C}^{18}\text{O}$ , the fractional abundance ranges from  $1 \times 10^{-8}$  to  $1.5 \times 10^{-7}$ . Similar to the  $^{13}\text{CO}$  abundance, it is small at some dense areas such as OMC-1/2/3 and L 1641 N.

Our map indicates that the fractional abundance varies from region to region within a factor of  $\sim 10$  (see figure 26). Toward the dense regions, the ratio seems to approach to  $\sim 5$ , close to the standard interstellar value. This variation may be partly related to the selective dissociation due to the

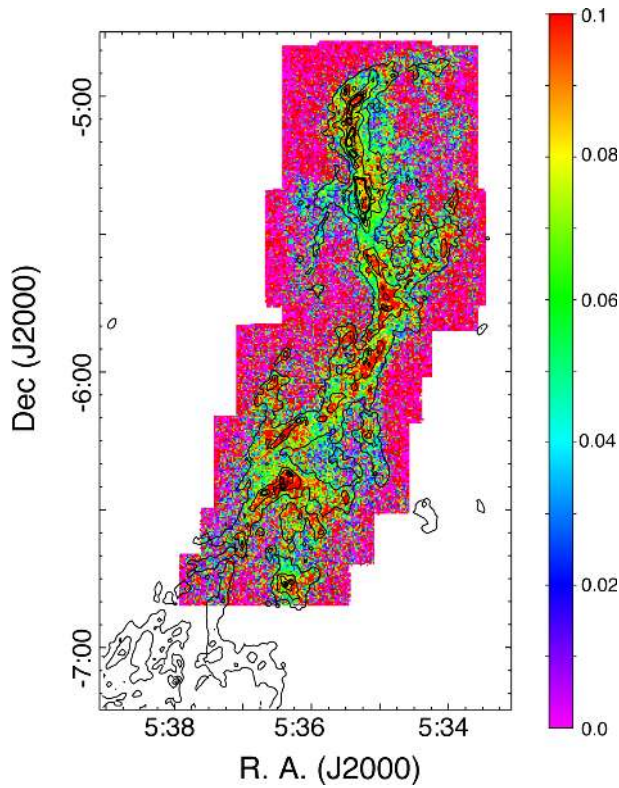


Fig. 26.  $^{13}\text{CO}$ -to- $\text{C}^{18}\text{O}$  fractional abundance ratio of Orion A. (Color online)

FUV radiation discussed by Shimajiri et al. (2011) and Ishii et al. (2019). See Ishii et al. (2018) for more details of the analysis.

In figure 27a we present the cumulative  $^{13}\text{CO}$  mass distributions of Orion A. We divide the cloud into three areas: North ( $\text{Dec} \geq -05:32:56.0$ ), OMC-1 ( $-05:30:26.0 \leq \text{Dec} \leq -05:16:03.5$ ), and South ( $\text{Dec} \leq -05:32:56.0$ ), where the North area includes OMC-1. This indicates that the OMC-1 area contains a fraction of molecular gas with column density higher than  $\sim 1 \text{ g cm}^{-2}$ , the threshold for high-mass star formation proposed by Krumholz and McKee (2008), beyond which further fragmentation of clouds can be avoided to form lower-mass cores, where  $\sim 1 \text{ g cm}^{-2}$  corresponds to a  $^{13}\text{CO}$  column density of  $\sim 5 \times 10^{17} \text{ cm}^{-2}$ , assuming a  $^{13}\text{CO}$  fractional abundance of  $2 \times 10^{-6}$  (Dickman 1978). In contrast, in the South, molecular gas with column densities higher than the threshold is deficient. The total  $^{13}\text{CO}$  mass is estimated to be  $3.9 \times 10^4 M_{\odot}$  with  $7.4 \times 10^3 M_{\odot}$ ,  $1.6 \times 10^4 M_{\odot}$ , and  $2.3 \times 10^4 M_{\odot}$  for OMC-1, North, and South, respectively.

Below, we repeat the same analysis for the other two regions.

### 6.1.2 Aquila Rift

Figure 28 shows the spatial distribution of the CO excitation temperature. The excitation temperature is high

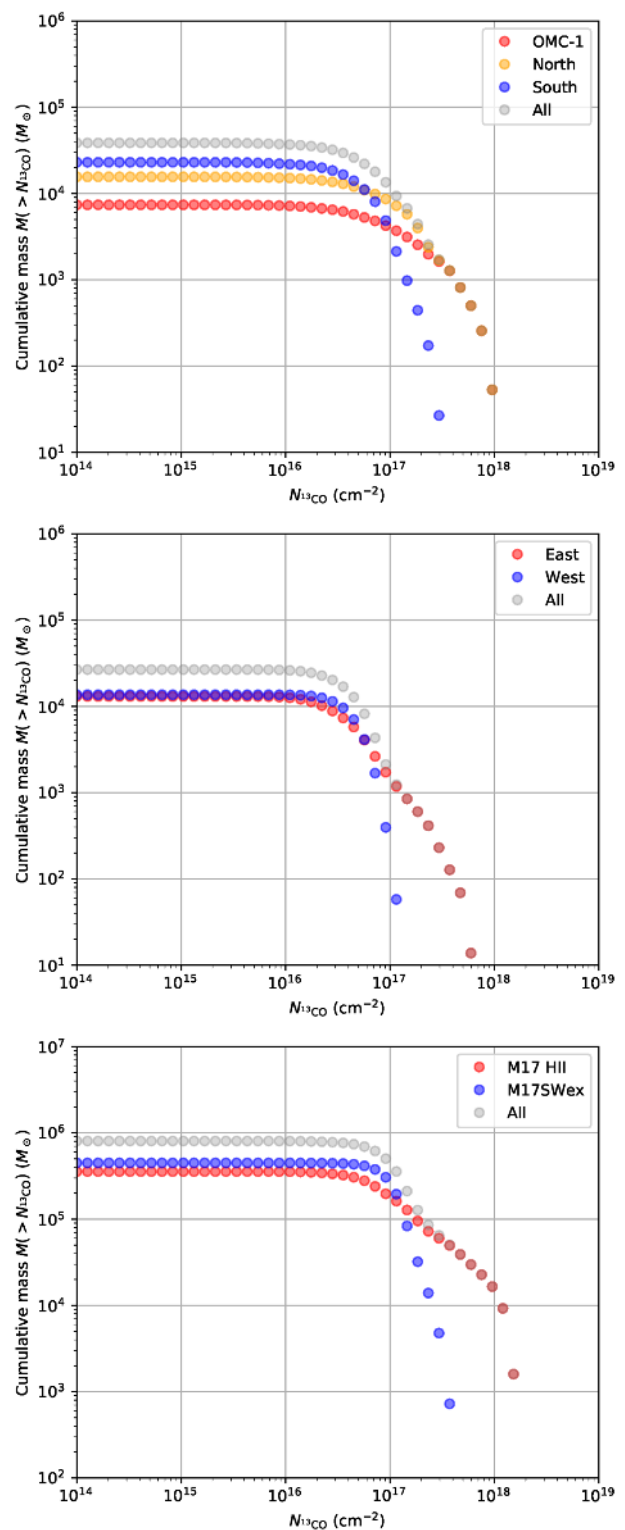


Fig. 27. Cumulative column density distributions in (a) Orion A, (b) Aquila Rift, and (c) M17. In Orion A, the area is divided into two (North and South) at  $\text{Dec} = -05:32:56.0$ . OMC-1 is a part of North and within  $-05:30:26.0 \leq \text{Dec} \leq -05:16:03.5$ . In the Aquila Rift, the area is divided into two (West and East) at  $\text{RA} = 18:30:39.6$ . In M17, the area is divided into two (HII and SWex) at  $l = 14:26:22.5$ . (Color online)

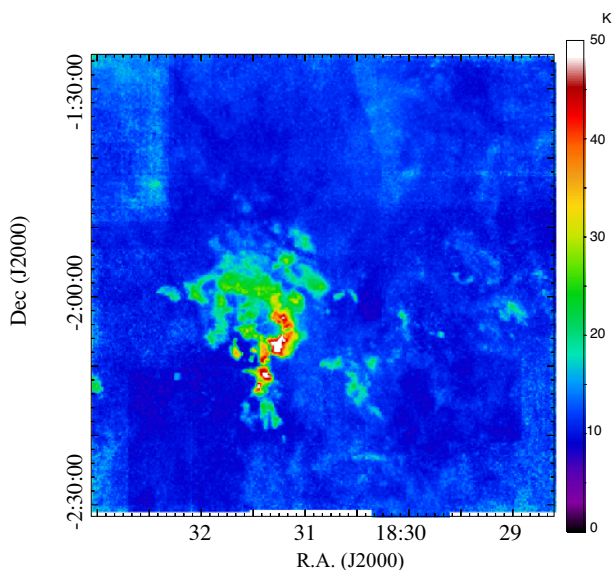


Fig. 28. Excitation temperature map of Aquila Rift. (Color online)

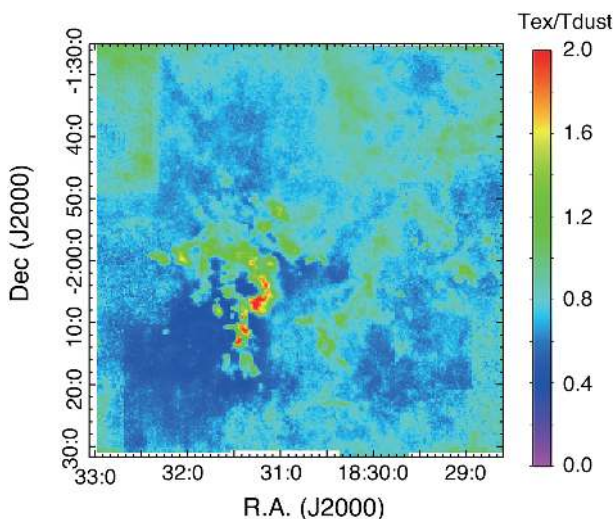


Fig. 29. The ratio of the excitation temperature derived from  $^{12}\text{CO}$  to the dust temperature derived from the Herschel data. The ratio stays at around unity in the molecular clouds. In W40, it goes up to  $\sim 2$ . (Color online)

toward the W 40 H II region. Serpens South has a relatively high excitation temperature of 25 K, but in other parts around Serpens South it is very low at  $\sim 10$  K, indicating that the star formation may not be active. In figure 29 we show the ratio of the excitation temperature derived from  $^{12}\text{CO}$  to the dust temperature. Here, we smoothed the excitation temperature map with an effective angular resolution of  $36''$  to match the effective resolution of the dust temperature map. The excitation temperature is nearly the same as the dust temperature in the Aquila Rift except in the W 40 H II region where the ratio goes up to about two.

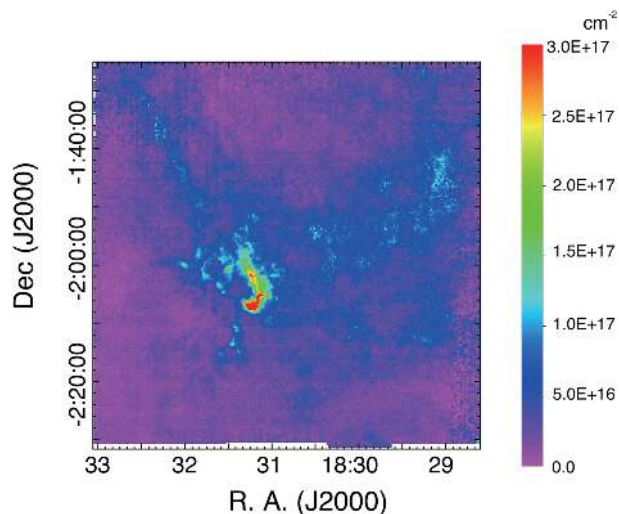


Fig. 30. The opacity-corrected  $^{13}\text{CO}$  column density map of Aquila Rift. (Color online)

Figures 30, 31, and 32 show the spatial distribution of the  $^{13}\text{CO}$  column density, the fractional abundances relative to  $\text{H}_2$ , and the optical depth for  $^{13}\text{CO}$  ( $J = 1-0$ ) and  $\text{C}^{18}\text{O}$  ( $J = 1-0$ ), respectively. The optical depth of  $^{13}\text{CO}$  tends to be higher than Orion A, and is sometimes larger than 2–3 toward the Serpens South region. The fractional abundances of  $^{13}\text{CO}$  and  $\text{C}^{18}\text{O}$  seem to be low in the filamentary structures seen in the Herschel map. This may indicate that CO molecules are depleted in the cold dense gas in Serpens South. The ratio of  $^{13}\text{CO}$  and  $\text{C}^{18}\text{O}$  abundances stays at around 0.1 (see figure 33).

In figure 27b we present the cumulative  $^{13}\text{CO}$  mass distributions of Aquila Rift. We divide the cloud into two areas: East ( $\text{Dec} \geq 18:30:39.6$ ) and West ( $\text{Dec} \leq 18:30:39.6$ ). This indicates that the Eastern area contains a fraction of molecular gas with column density higher than  $\sim 1 \text{ g cm}^{-2}$ , the threshold for high-mass star formation proposed by Krumholz and McKee (2008). In contrast, in the Western area which contains Serpens South, the molecular gas with column densities higher than the threshold is deficient. The total  $^{13}\text{CO}$  mass is estimated to be  $3.9 \times 10^4 M_\odot$  with  $7.4 \times 10^3 M_\odot$ ,  $1.6 \times 10^4 M_\odot$ , and  $2.3 \times 10^4 M_\odot$  for OMC-1, North, and South, respectively.

## 6.2 M 17

Figure 34 shows the spatial distribution of the CO excitation temperature. The excitation temperature is high toward the M 17 H II region. In contrast, in the infrared dark cloud the excitation temperature stays at 30–40 K. The excitation temperatures are not so low as those of the Serpens South region. Figures 35 and 36 show the spatial distribution of the column density and the optical depth

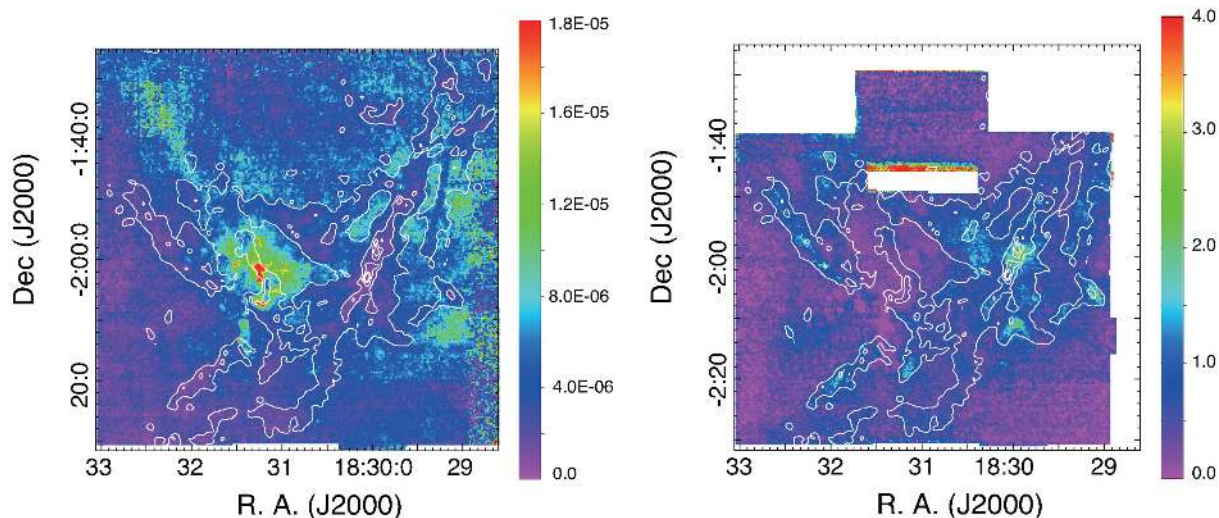


Fig. 31. (a)  $^{13}\text{CO}$  fractional abundance and (b) its optical depth maps of Aquila Rift. (Color online)

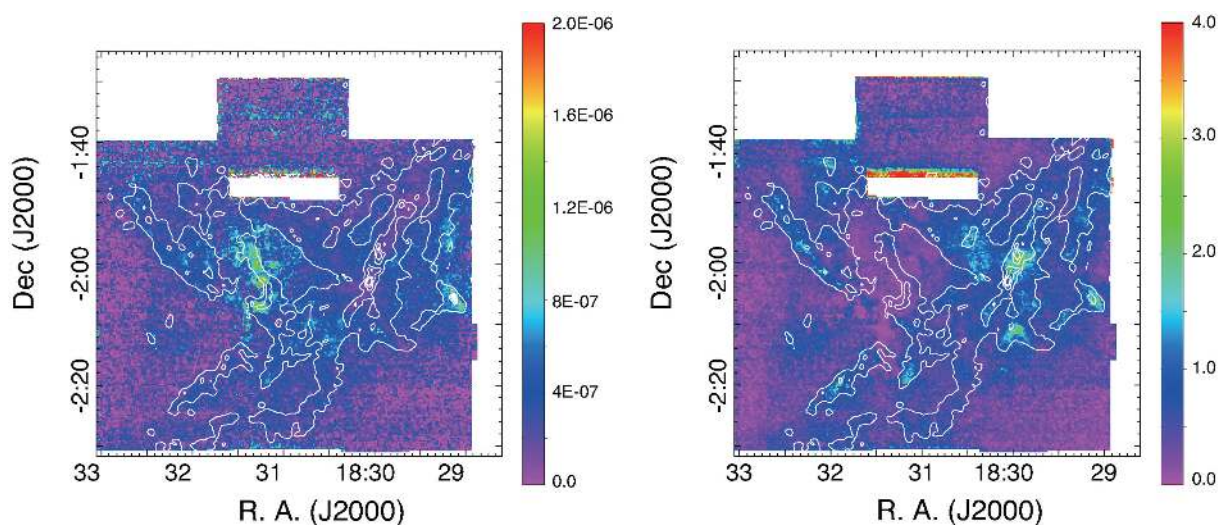


Fig. 32. (a)  $\text{C}^{18}\text{O}$  fractional abundance and (b) its optical depth maps of Aquila Rift. (Color online)

for  $^{13}\text{CO}$  ( $J = 1-0$ ) and  $\text{C}^{18}\text{O}$  ( $J = 1-0$ ), respectively. The optical depths of  $^{13}\text{CO}$  and  $\text{C}^{18}\text{O}$  tend to be higher toward M17 SWex. See Nuygen Luong et al. (2019) for details of the global molecular gas distributions.

In figure 27c we present the cumulative  $^{13}\text{CO}$  mass distributions of M17. We divide the region into two areas: the M17 HII area ( $l \geq 14.9$ ) and M17 SWex ( $l \leq 14.9$ ). This indicates that the M17 HII region contains a fraction of molecular gas with column density higher than  $\sim 1 \text{ g cm}^{-2}$ , the threshold for high-mass star formation proposed by Krumholz and McKee (2008). In contrast, for M17 SWex molecular gas with column densities higher than the threshold is deficient. This may be a reason why high-mass star formation is not active in M17 SWex (Povich et al. 2016). The total  $^{13}\text{CO}$  mass is estimated to be  $3.6 \times 10^5 M_{\odot}$  and  $4.5 \times 10^5 M_{\odot}$  for M17 HII and M17

SWex, respectively. The M17 SWex area contains about twice as much massive molecular gas than M17 HII.

## 7 Molecular outflows

Molecular outflow feedback is an important stellar feedback mechanism (Nakamura & Li 2007, 2014). Molecular outflows can inject significant energy and momentum into molecular clouds. Our  $^{12}\text{CO}$  data are useful to identify the outflows and gauge how much energy and momentum are injected into the clouds. A molecular outflow survey is one of the main studies we will conduct. Here we briefly present the result of the molecular outflow survey toward small areas in Orion A (L1641 N) and the Aquila Rift (Serpens South). See Tanabe et al. (2019) for the results of comprehensive outflow surveys toward Orion A.



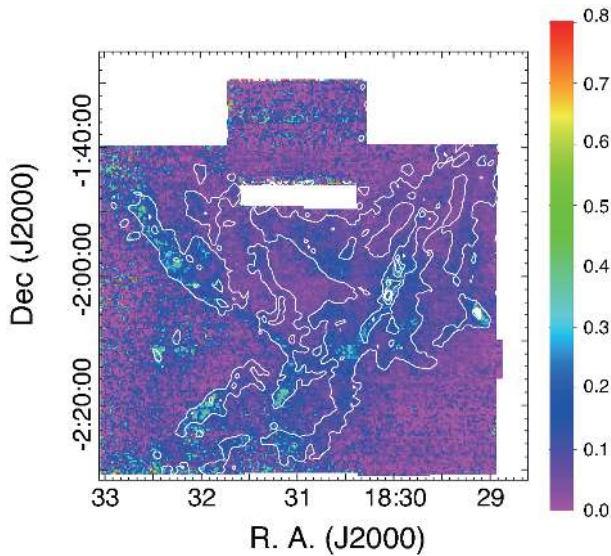


Fig. 33.  $C^{18}O$ -to- $^{13}CO$  fractional abundance ratio of Aquila Rift. (Color online)

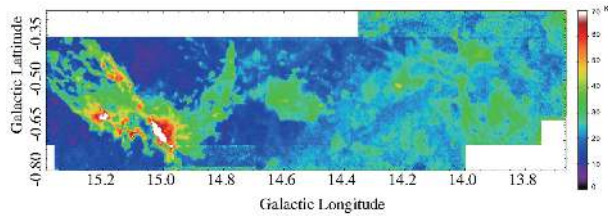


Fig. 34. Excitation temperature map of M 17. (Color online)

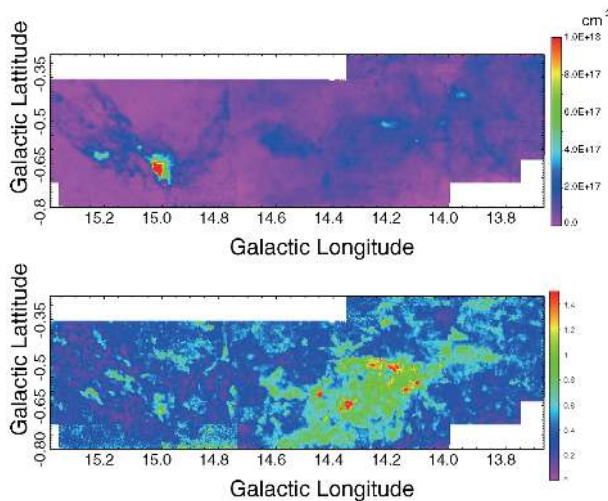


Fig. 35. (a)  $^{13}CO$  fractional abundance and (b) its optical depth maps of M 17. (Color online)

## 7.1 Orion A (L 1641 N)

In figure 38 we present a three-color image of the L 1641 N region. The red, blue, and green images show the  $^{12}CO$  intensity image integrated from  $11 \text{ km s}^{-1}$  to  $15 \text{ km s}^{-1}$  (redshifted component),  $^{12}CO$  intensity image integrated

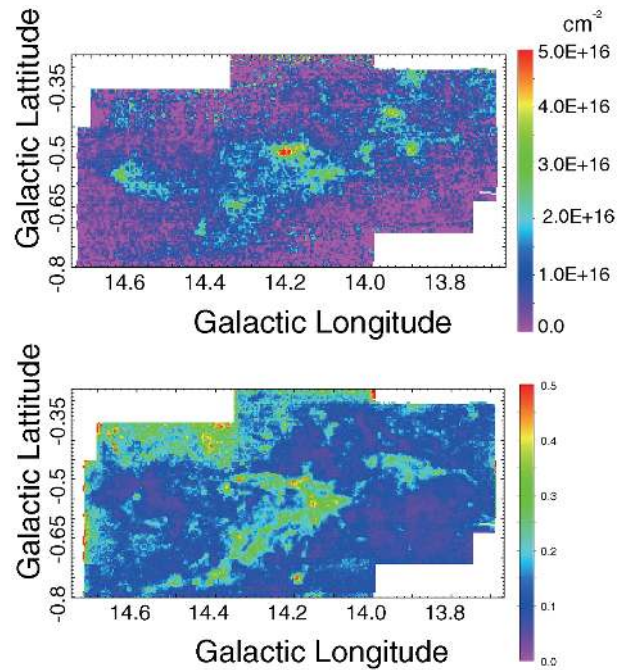


Fig. 36. (a)  $C^{18}O$  fractional abundance and (b) its optical depth maps of M 17. (Color online)

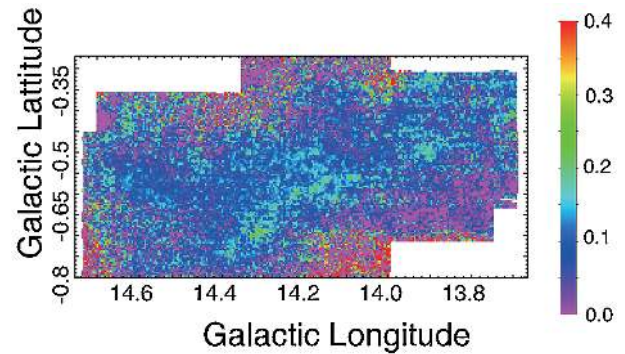
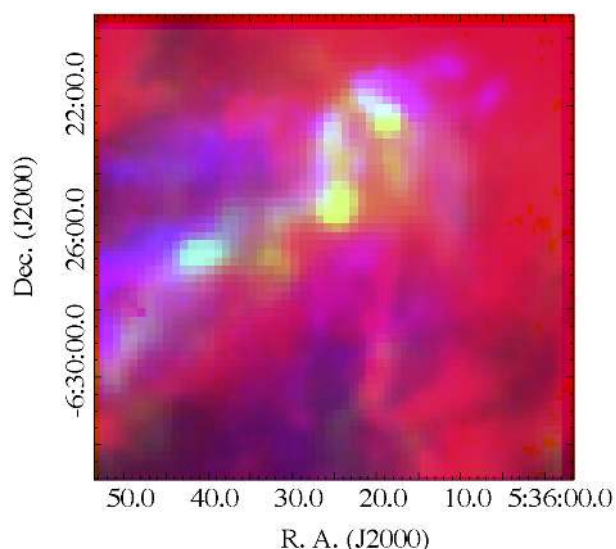


Fig. 37.  $C^{18}O$ -to- $^{13}CO$  fractional abundance ratio of M 17. (Color online)

from  $-20 \text{ km s}^{-1}$  to  $0 \text{ km s}^{-1}$  (blueshifted components), and the Herschel column density image, respectively. In this region, Stanke and Williams (2007) and Nakamura et al. (2012) identified molecular outflows in  $^{12}CO (J = 2-1)$  and  $^{12}CO (J = 1-0)$ , respectively. The high-velocity components they previously identified are recognized in our image. For example, there are several dust cores in this region, shown in green. The redshifted collimated flow running from north to south blows out from the brightest dust core located at the position (RA, Dec) = (5:36:19, -6:22:29).

The result of accurate outflow identification is presented in Tanabe et al. (2019), who found 44 CO outflows in Orion A, 17 of which are new detections. Based on the identified outflow physical parameters, they estimated the momentum injection rates due to the molecular outflows and found that the total momentum injection rate due to



**Fig. 38.** Three-color image of the L 1641 N cluster-forming region with  $^{12}\text{CO}$  ( $J = 1-0$ ) intensity integrated from  $10\text{ km s}^{-1}$  to  $16\text{ km s}^{-1}$  (red),  $^{12}\text{CO}$  ( $J = 1-0$ ) intensity integrated from  $0\text{ km s}^{-1}$  to  $5\text{ km s}^{-1}$  (blue), and the Herschel column density (green). (Color online)

the outflows and the expanding shells identified in the  $^{13}\text{CO}$  data by Feddersen et al. (2018) is larger than the turbulence dissipation rate in Orion A. Thus, the stellar feedback such as molecular outflows and expanding shells driven by stellar winds is an important mechanism to replenish the internal cloud turbulence.

## 7.2 Aquila Rift (Serpens South)

In figure 39 we present the three-color image of the Serpens South region. Nakamura et al. (2011a) conducted a molecular outflow survey toward the Serpens South cluster in  $^{12}\text{CO}$  ( $J = 3-2$ ). The present paper is the first outflow survey using  $^{12}\text{CO}$  ( $J = 1-0$ ). The coverage of the image shown in figure 39 is wider than that of Nakamura et al. (2011a). The red, blue, and green images indicate the  $^{12}\text{CO}$  intensity image integrated from  $11\text{ km s}^{-1}$  to  $15\text{ km s}^{-1}$  (redshifted component), the  $^{12}\text{CO}$  intensity image integrated from  $-20\text{ km s}^{-1}$  to  $0\text{ km s}^{-1}$  (blueshifted components), and the Herschel column density image, respectively. The distribution of the high-velocity components is basically similar to that of  $^{12}\text{CO}$  ( $J = 3-2$ ).

By visual inspection, we attempted to identify the high-velocity components that are likely to originate from the molecular outflows toward Herschel protostellar cores in this region. The result of the identification is summarized in table 10. We detected in the  $^{12}\text{CO}$  ( $J = 1-0$ ) emission almost all the outflow lobes identified by Nakamura et al. (2011a). In total, we identified 13 outflow driving sources including the 3 tentative detections. From this survey, we

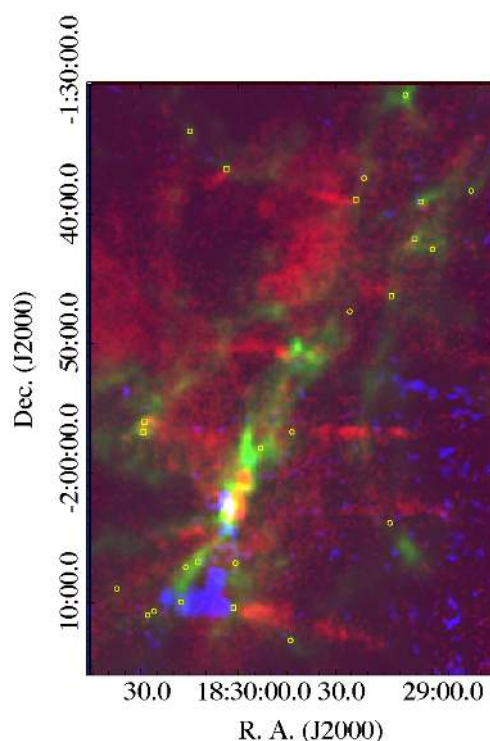


**Fig. 39.** Three-color image of the Serpens South region with  $^{12}\text{CO}$  ( $J = 1-0$ ) intensity integrated from  $11\text{ km s}^{-1}$  to  $15\text{ km s}^{-1}$  (red),  $^{12}\text{CO}$  ( $J = 1-0$ ) intensity integrated from  $-20\text{ km s}^{-1}$  to  $0\text{ km s}^{-1}$  (blue), and the Herschel column density (green). The squares and circles indicate protostellar core candidates with and without molecular outflows, respectively. The size of the circle is the same as the FWHM beam size of  $21''.7$ . (Color online)

identified 4 new outflow sources, all of which are located outside the map of Nakamura et al. (2011a).

As discussed by Shimoikura et al. (2015), the Aquila Rift region contains several cloud components with different line-of-sight velocities. The existence of such multiple components sometimes precludes clear identification of high-velocity components, since high-velocity components tend to overlap with different cloud components along the line of sight. More careful inspection of the data cube is needed to fully identify the molecular outflows. We expect that more outflows exist even in the area presented here. We will present a complete outflow survey toward the Aquila Rift in a separate paper.

The scientific results will be reported in more detail in separate papers.

## 8 Summary

In the present paper we have provided a project overview of the Nobeyama mapping project toward the three nearby molecular clouds Orion A, Aquila Rift, and M17. The main purpose of the present paper is to summarize the complicated observational procedures and flux calibration

**Table 10.** Molecular outflow candidates in Serpens South.\*

No.	RA (J2000.0)	Dec (J2000.0)	Outflows	Classification	Nakamura et al. (2011a)
135	18:28:48.09	-01:38:11.6	N		
147	18:29:00.01	-01:42:42.8	N		
151	18:29:03.62	-01:39:03.0	BR	C	B12, R7
155	18:29:05.52	-01:41:53.6	R	C	B11, R6
163	18:29:08.34	-01:30:46.8	N		
171	18:29:12.68	-01:46:18.4	R	M	new
174	18:29:13.10	-02:03:51.2	N		
196	18:29:21.13	-01:37:12.8	N		
202	18:29:23.69	-01:38:54.0	R	C	B10, R5
209	18:29:25.54	-01:47:31.5	N		
250	18:29:43.44	-01:56:49.9	N		
251	18:29:43.84	-02:12:56.0	N		
271	18:29:53.06	-01:58:04.5	N		
285	18:29:59.67	-02:00:58.7	R	C	R2
289	18:30:00.85	-02:06:57.3	N		
290	18:30:01.20	-02:06:09.8	N		
292	18:30:01.50	-02:10:25.5	BR	C	B15, R8
297	18:30:03.68	-01:36:29.4	R	C	new
299	18:30:04.19	-02:03:05.5	BR	C	B1, B2, B3, B6, R1, R3, R4?
315	18:30:12.44	-02:06:53.6	B	C	B7
321	18:30:14.93	-01:33:34.9	BR	M	new
323	18:30:16.22	-02:07:16.3	N		
326	18:30:17.64	-02:09:59.3	B	C	B14
342	18:30:26.03	-02:10:41.2			
347	18:30:27.97	-02:10:59.0			
349	18:30:28.98	-01:56:03.2	R	Y	R9
351	18:30:29.28	-01:56:50.6	R	M	new
362	18:30:37.53	-02:08:56.3	N	N	

\*First column: the number in the Herschel protostellar core catalog of Könyves et al. (2015). Fourth column: B = blueshifted component, R = redshifted component. Fifth column: C = clear, M = marginal. Sixth column: comparison with the identification by Nakamura et al. (2011a); new = new detection (this paper). In the densest part of the Serpens South cluster, outflow components from several different sources are observed. We assigned all such lobes to No. 299.

methods. We summarize the main results of the paper as follows.

1. We conducted wide-field mapping observations toward three nearby molecular clouds, Orion A, Aquila Rift, and M 17, in  $^{12}\text{CO}$  ( $J = 1-0$ ),  $^{13}\text{CO}$  ( $J = 1-0$ ),  $\text{C}^{18}\text{O}$  ( $J = 1-0$ ),  $\text{N}_2\text{H}^+$  ( $J = 1-0$ ), and  $\text{CCS}$  ( $J_N = 8_7-7_6$ ) using the Nobeyama 45 m telescope.
2. The map coverage is over  $1^\circ \times 1^\circ$ . We cover most of the molecular clouds seen in dust emission.
3. We checked the absolute intensities obtained with the new four-beam receiver, FOREST, by comparing the intensities obtained with the previous receiver, BEARS, toward the same areas for  $^{12}\text{CO}$ ,  $^{13}\text{CO}$ , and  $\text{C}^{18}\text{O}$ .
4. For  $\text{N}_2\text{H}^+$ , we compared our results with the intensities of the Taurus molecular cloud obtained with the IRAM 30 m telescope; the fluxes taken with FOREST coincide with those obtained with the IRAM 30 m telescope within an error of 5%.

5. We obtained the column densities of  $^{13}\text{CO}$  ( $J = 1-0$ ) and  $\text{C}^{18}\text{O}$  ( $J = 1-0$ ) and derived their fractional abundances toward Orion A. Our maps indicate that the fractional abundances depend on the cloud environments, and vary from region to region by a factor of  $\sim 10$ .
6. The cumulative column density distributions clearly show that only a fraction of the molecular gas has column densities high enough to create high-mass stars for individual clouds.
7. Our maps have sufficient sensitivities to identify the molecular outflows. In particular, in our  $^{12}\text{CO}$  ( $J = 1-0$ ) data, we confirmed all the outflows previously detected in  $^{12}\text{CO}$  ( $J = 3-2$ ) toward Serpens South, and identified four new outflows in the adjacent region. Using the catalog of the protostars, we identified the driving sources of these CO outflows.
8. Finally, we briefly described results from our project published in separate papers. We revealed the hierarchical

structure of Orion A, applying SCIMES and Dendrogram to the  $^{13}\text{CO}$  cube data. In total, we identified about 80 clouds in Orion A. The abundance ratio of  $^{13}\text{CO}$  to  $\text{C}^{18}\text{O}$  varies from region to region, affected by the far-UV radiation (Ishii et al. 2019). We identified 44 outflows in Orion A, 15 of which are new detections (Tanabe et al. 2019). We estimated the momentum injection rate of the identified outflows and found that they have significant injection momentum rates in the surroundings. Using the data of the OMC-2 FIR 4 region, we characterized the spatial variation of the abundance ratios of several molecules and discussed possible outflow-triggered star formation (Nakamura et al. 2019). Data was taken for the flux calibration of Orion A data. For Aquila, Shimoikura et al. (2019b) reveal evidence of the interaction of the molecular cloud with the expanding H II region. Kusune et al. (2019) and Sugitani et al. (2019) carried out near-infrared polarization observations toward Aquila (see also Sugitani et al. 2011) and M17, respectively, and reveal that the global magnetic field tends to be perpendicular to the elongation of the molecular clouds. Nguyen Luong et al. (2019) and Shimoikura et al. (2019b) reveal the global molecular gas distribution in M17, and found that in the IRDC region, the column densities are not dense enough to create high-mass stars, but ongoing cloud–cloud collisions are likely to be forming higher-density regions. Thus, future high-mass star formation is expected.

## Acknowledgments

This work was financially supported by JSPS KAKENHI Grant Numbers JP16H05730, JP17H02863, JP17H01118, JP26287030, JP17K00963, JP17H01103, JP18H05441, and JP18H01259. This work was supported by NAOJ ALMA Scientific Research Grant Numbers 2017-04A. This work was carried out as one of the large projects of the Nobeyama Radio Observatory (NRO), which is a branch of the National Astronomical Observatory of Japan, National Institute of Natural Sciences. We thank the NRO staff for both operating the 45 m and helping us with the data reduction.

## References

- André, P., et al. 2010, *A&A*, 518, L102  
 Arce, H. G., Borkin, M. A., Goodman, A. A., Pineda, J. E., & Beaumont, C. N. 2011, *ApJ*, 742, 105  
 Bally, J. 2016, *ARA&A*, 54, 491  
 Berné, O., Marcelino, N., & Cernicharo, J. 2014, *ApJ*, 795, 13  
 Breitschwerdt, D., Egger, R., Freyberg, M. J., Frisch, P. C., & Vallerga, J. V. 1996, *Space Sci. Rev.*, 78, 183  
 Buckle, J. V., et al. 2012, *MNRAS*, 422, 521  
 Caselli, P., Benson, P. J., Myers, P. C., & Tafalla, M. 2002, *ApJ*, 572, 238  
 Chen, H.-R. V., et al. 2019, *ApJ*, 875, 24  
 Da Rio, N., et al. 2016, *ApJ*, 818, 59  
 Dame, T. M., Hartmann, D., & Thaddeus, P. 2001, *ApJ*, 547, 792  
 Dickman, R. L. 1978, *ApJS*, 37, 407  
 Dobashi, K. 2011, *PASJ*, 63, S1  
 Dobashi, K., Shimoikura, T., Endo, N., Takagi, C., Nakamura, F., Shimajiri, Y., & Bernard, J.-P. 2019a, *PASJ*, 71, S11  
 Dobashi, K., Shimoikura, T., Katakura, S., Nakamura, F., & Shimajiri, Y. 2019b, *PASJ*, 71, S12  
 Dobashi, K., Uehara, H., Kandori, R., Sakurai, T., Kaiden, M., Umamoto, T., & Sato, F. 2005, *PASJ*, 57, 417  
 Elmegreen, B. G. 1979, *ApJ*, 232, 729  
 Evans, N. J., II, et al. 2009, *ApJS*, 181, 321  
 Feddersen, J. R., et al. 2018, *ApJ*, 862, 121  
 Frisch, P. C. 1998, in *IAU Coll. 166, The Local Bubble and Beyond*, ed. D. Breitschwerdt et al. (Berlin: Springer-Verlag), 269  
 Frisch, P. C., et al. 2015, *J. Phys.: Conf. Ser.*, 577, 012010  
 Goicoechea, J. R., Santa-Maria, M. G., Bron, E., Teyssier, D., Marcelino, N., Cernicharo, J., & Cuadrado, S. 2019, *A&A*, 622, A91  
 Gutermuth, R. A., et al. 2008, *ApJ*, 673, L151  
 Hacar, A., Alves, J., Tafalla, M., & Goicoechea, J. R. 2017, *A&A*, 602, L2  
 Ikeda, N., Sunada, K., & Kitamura, Y. 2007, *ApJ*, 665, 1194  
 Ishii, S., et al. 2016, *PASJ*, 68, 10  
 Ishii, S., Nakamura, F., Shimajiri, Y., Kawabe, R., Tsukagoshi, T., Dobashi, K., & Shimoikura, T. 2019, *PASJ*, 71, S9  
 Kim, M. K., et al. 2008, *PASJ*, 60, 991  
 Kirk, H., Myers, P. C., Bourke, T. L., Gutermuth, R. A., Hedden, A., & Wilson, G. W. 2013, *ApJ*, 766, 115  
 Klessen, R. S., Burkert, A., & Bate, M. R. 1998, *ApJ*, 501, L205  
 Kong, S., et al. 2018, *ApJS*, 236, 25  
 Könyves, V., et al. 2015, *A&A*, 584, A91  
 Krumholz, M. R., et al. 2014, in *Protostars and Planets VI*, ed. H. Beuther et al. (Tucson: University of Arizona Press), 243  
 Krumholz, M. R., & McKee, C. F. 2008, *Nature*, 451, 1082  
 Krumholz, M. R., & Tan, J. C. 2007, *ApJ*, 654, 304  
 Kuhn, M. A., Feigelson, E. D., Getman, K. V., Sills, A., Bate, M. R., & Borissova, J. 2015, *ApJ*, 812, 131  
 Kusune, T., et al. 2019, *PASJ*, 71, S5  
 Lin, S.-J., et al. 2016, *ApJ*, 826, 193  
 Loinard, L., Torres, R. M., Mioduszewski, A. J., Rodríguez, L. F., González-Lópezlira, R. A., Lachaume, R., Vázquez, V., & González, E. 2007, *ApJ*, 671, 546  
 Loison, J.-C., Wakelam, V., & Hickson, K. M. 2014, *MNRAS*, 443, 398  
 Lombardi, M., Bouy, H., Alves, J., & Lada, C. J. 2014, *A&A*, 568, C1  
 Mac Low, M.-M., & Klessen, R. S. 2004, *Rev. Mod. Phys.*, 76, 125  
 McKee, C. F., & Ostriker, E. C. 2007, *ARA&A*, 45, 565  
 McKee, C. F., & Williams, J. P. 1997, *ApJ*, 476, 144  
 Marka, C., Schreyer, K., Launhardt, R., Semenov, D. A., & Henning, T. 2012, *A&A*, 537, A4  
 Maruta, H., Nakamura, F., Nishi, R., Ikeda, N., & Kitamura, Y. 2010, *ApJ*, 714, 680  
 Maury, A. J., André, P., Men'shchikov, A., Könyves, V., & Bontemps, S. 2011, *A&A*, 535, A77  
 Megeath, S. T., et al. 2012, *AJ*, 144, 192

- Meingast, S., et al. 2016, *A&A*, 587, A153
- Menten, K. M., Reid, M. J., Forbrich, J., & Brunthaler, A. 2007, *A&A*, 474, 515
- Minamidani, T., et al. 2016, *SPIE Proc.*, 9914, 99141Z
- Murray, N., & Rahman, M. 2010, *ApJ*, 709, 424
- Nakamura, F., et al. 2011a, *ApJ*, 726, 46
- Nakamura, F., et al. 2011b, *ApJ*, 737, 56
- Nakamura, F., et al. 2012, *ApJ*, 746, 25
- Nakamura, F., et al. 2014, *ApJ*, 791, L23
- Nakamura, F., et al. 2019, *PASJ*, 71, S10
- Nakamura, F., Dobashi, K., Shimoikura, T., Tanaka, T., & Onishi, T. 2017, *ApJ*, 837, 154
- Nakamura, F., & Li, Z.-Y. 2007, *ApJ*, 662, 395
- Nakamura, F., & Li, Z.-Y. 2014, *ApJ*, 783, 115
- Nishimura, A., et al. 2015, *ApJS*, 216, 18
- Nishimura, A., et al. 2018, *PASJ*, 70, S42
- Nguyen Luong, Q., Nakamura, F., Shimoikura, T., Sugitani, K., Dobashi, K., Kim, K.-T., Kang, H., & Evans, N. 2019, *PASJ*, submitted
- Ohashi, S., Sanhueza, P., Chen, H.-R. V., Zhang, Q., Busquet, G., Nakamura, F., Palau, A., & Tatematsu, K. 2016, *ApJ*, 833, 209
- Ortiz-León, G. N., et al. 2017a, *ApJ*, 834, 141
- Ortiz-León, G. N., et al. 2017b, *ApJ*, 834, 143
- Pabst, C., et al. 2019, *Nature*, 565, 618
- Pagani, L., Daniel, F., & Dubernet, M.-L. 2009, *A&A*, 494, 719
- Pineda, J. E., Caselli, P., & Goodman, A. A. 2008, *ApJ*, 679, 481
- Povich, M. S., et al. 2006, *ApJ*, 696, 1278
- Povich, M. S., Townsley, L. K., Robitaille, T. P., Broos, P. S., Orbin, W. T., King, R. R., Naylor, T., & Whitney, B. A. 2016, *ApJ*, 825, 125
- Povich, M. S., & Whitney, B. A. 2010, *ApJ*, 714, L285
- Punanova, A., et al. 2016, *A&A*, 587, 118
- Ripple, F., Heyer, M. H., Gutermuth, R., Snell, R. L., & Brunt, C. M. 2013, *MNRAS*, 431, 1296
- Robitaille, T. P., & Whitney, B. A. 2010, *ApJ*, 710, L11
- Rumble, D., et al. 2016, *MNRAS*, 460, 4150
- Sawada, T., et al. 2008, *PASJ*, 60, 445
- Shimajiri, Y., et al. 2011, *PASJ*, 63, 105
- Shimajiri, Y., et al. 2014, *A&A*, 564, A68
- Shimajiri, Y., et al. 2015, *ApJS*, 217, 7
- Shimajiri, Y., et al. 2017, *A&A*, 604, A74
- Shimoikura, T., Dobashi, K., Hirose, A., Nakamura, F., Shimajiri, Y., & Sugitani, K. 2019a, *PASJ*, 71, S6
- Shimoikura, T., Dobashi, K., Nakamura, F., Hara, C., Tanaka, T., Shimajiri, Y., Sugitani, K., & Kawabe, R. 2015, *ApJ*, 806, 201
- Shimoikura, T., Dobashi, K., Nakamura, F., Matsumoto, T., & Hirota, T. 2018, *ApJ*, 855, 45
- Shimoikura, T., Dobashi, K., Nakamura, F., Shimajiri, Y., & Sugitani, K. 2019b, *PASJ*, 71, S4
- Shu, F. H., Adams, F. C., & Lizano, S. 1987, *ARA&A*, 25, 23
- Stanke, T., & Williams, J. P. 2007, *AJ*, 133, 1307
- Sugitani, K., et al. 2011, *ApJ*, 734, 63
- Sugitani, K., et al. 2019, *PASJ*, 71, S7
- Suzuki, H., Yamamoto, S., Ohishi, M., Kaifu, N., Ishikawa, S.-I., Hirahara, Y., & Takano, S. 1992, *ApJ*, 392, 551
- Tafalla, M., & Hacar, A. 2015, *A&A*, 574, A104
- Takahashi, S., Saito, M., Ohashi, N., Kusakabe, N., Takakuwa, S., Shimajiri, Y., Tamura, M., & Kawabe, R. 2008, *ApJ*, 688, 344
- Tanabe, Y., et al. 2019, *PASJ*, 71, S8
- Tanaka, T., et al. 2013, *ApJ*, 778, 34
- Tatematsu, K., et al. 2014, *PASJ*, 66, 16
- Tatematsu, K., Kandori, R., Umamoto, T., & Sekimoto, Y. 2008, *PASJ*, 60, 407
- Torres, R. M., Loinard, L., Mioduszewski, A. J., & Rodríguez, L. F. 2007, *ApJ*, 671, 1813
- Wilson, B. A., Dame, T. M., Mashed, M. R. W., & Thaddeus, P. 2005, *A&A*, 430, 523
- Xu, Y., Moscadelli, L., Reid, M. J., Menten, K. M., Zhang, B., Zheng, X. W., & Brunthaler, A. 2011, *ApJ*, 733, 25
- Yoshida, A., Kitamura, Y., Shimajiri, Y., & Kawabe, R. 2010, *ApJ*, 718, 1019
- Zucker, C., Battersby, C., & Goodman, A. 2015, *ApJ*, 815, 23
- Zuckerman, B., & Evans, N. J., II 1974, *ApJ*, 192, L149